Biomass and Bioenergy xxx (xxxx) xxx

Contents lists available at ScienceDirect

Biomass and Bioenergy

journal homepage: www.elsevier.com/locate/biombioe

Biomass pyrolysis over ZIF-67 catalyst: thermogravimetric, pyrolysis vapors, kinetics, thermodynamics and artificial neural network modelling

Samy Yousef [a,*], Vilmantė Kudelytė [b], Nerijus Striūgas [b], Mohammed Ali Abdelnaby [c]

[a] Department of Production Engineering, Faculty of Mechanical Engineering and Design, Kaunas University of Technology, Kaunas, LT-51424, Lithuania
[b] Lithuanian Energy Institute, Laboratory of Combustion Processes, Breslaujos 3, Kaunas, LT-44403, Lithuania
[c] Mechatronics Systems Engineering Department, October University for Modern Sciences and Arts-MSA, Giza, Egypt

ARTICLE INFO

Keywords:
Metal-organic frameworks
Zeolitic imidazolate frameworks
Catalytic pyrolysis
Kinetics
Artificial neural networks

ABSTRACT

Zeolite Imidazole Frame-67 (ZIF-67), a thermally stable subclass of metal-organic frameworks (MOFs), has recently emerged as a promising flexible catalyst for upgrading biomass pyrolysis process and reducing reaction complexity. This research explores the catalytic pyrolysis behavior of wood pellets (WP) biomass over ZIF-67 using thermogravimetric analysis (TGA), TG-Fourier Transform Infrared (TG-FTIR) spectroscopy, and gas chromatography-mass spectrometry (GC-MS). Thermal decomposition kinetics and thermodynamic parameters were evaluated using serval modelling approaches, while artificial neural network (ANN) technique was employed to predict pyrolysis behaviour of WP and ZIF-67/WP samples under untested conditions. Biomass samples containing 10, 20 and 30 wt% ZIF-67 were examined to determine the optimum catalyst loading. The TGA results revealed that biomass underwent thermal decomposition below 600 °C, with a mass loss of 77-86 wt %, followed by the decomposition of ZIF-67 at higher temperatures. The addition of ZIF-67 significantly influenced the composition of the evolved vapors, with 20 wt% catalyst providing the highest catalytic activity by promoting the formation of naphthalene, 1,2,3,4 tetrahydro-2-phenyl-rich vapor, which accounted for approximately 85% of the total identified aromatic GC-MC peak area under the investigated conditions. Kinetics analysis demonstrated that the optimum ZIF-67 loading reduced the activation energy from 233 to 427 kJ/mol (WP) to 159-295 kJ/mol, indicating a substantial reduction in the energy barrier of pyrolysis. Furthermore, the catalyst lowered thermodynamics parameters (enthalpy, Gibbs free energy, and entropy), confirming improved reaction feasibility. The constructed ANN models accurately predicted the pyrolysis behaviour of both WP and ZIF-67/WP samples, achieving R^2 exceeding 0.9999. These results demonstrate that incorporating 20 wt% of ZIF-67 into the biomass pyrolysis process effectively reduces the reaction energy requirements and enhances the selectivity of pyrolysis vapors towards valuable aromatic hydrocarbons, highlighting its potential as an efficient catalyst for sustainable biomass valorisation and the production of advanced biofuels and renewable chemicals.

1. Introduction

In the context of efforts to find new, alternative and renewable energy sources to reduce dependence on fossil fuels and mitigate their emissions, biomass, as a renewable feedstock, has gained considerable attention in this regard due to its high availability, estimated at more than one billion tons in the European Union region alone [1]. This is further enhanced by the diversity of its production sources, including wood (chips, sawdust), agricultural residues (crop residues, straw, etc.), forests, and others [2]. Biomass consists of organic components (cellulose (25-50 wt%), hemicellulose (15-40 wt%), lignin (10-40 wt%), and various carbohydrates) [3], making it one of the most promising low-emission renewable energy alternatives and biofuel production [4]. Among the reported biomass sources, wood is the most abundant, constituting over 50% of plant biomass, the woody material that forms the basic structure of forests [5]. Based on the current situation, biomass conversion technologies are varying between thermochemical (pyrolysis, hydrothermal liquefaction, gasification, combustion, torrefaction, incineration), biological (fermentation, anaerobic digestion, aerobic composting), biochemical (hydrolysis, transesterification, supercritical water gasification), and physical (briquetting, extraction, distillation) [6]. Among these pathways, thermochemical approach, particularly

* Corresponding author.
E-mail address: ahmed.saed@ktu.lt (S. Yousef).

https://doi.org/10.1016/j.biombioe.2026.109868
Received 30 June 2026; Received in revised form 17 July 2026; Accepted 18 July 2026

using pyrolysis, has shown tremendous potential in converting biomass into biofuels (bio-oil and biogas) and renewable chemical compounds. Also, the studies have demonstrated its sustainability and superior environmental and economic performance compared to other conversion technologies [7–9]. However, this approach still faces several challenges, including the high viscosity and water content of the resulting bio-oil, its low calorific value, corrosive nature due to high acidity, and the abundance of oxygenated compounds [10]. These characteristics negatively affect fuel quality and stability, hindering its integration into the market for commercially viable biofuels [11]. In addition, this approach is accompanied by the production of large quantities of biochar as a by-product with limited applications and less economic value [12,13]. These shortages resulted from the complexity of biomass structure with its high carbon and low hydrogen content that make it hard to decompose into oil and favouring the formation of biochar over oil production [14]. To mitigate this problem and achieve efficient biomass decomposition, upgrading processes using catalytic pyrolysis are commonly employed to improve the properties of bio-oil, including reducing its acidity and viscosity. This process also removes oxidizing agents and impurities and reduce the reaction complexity. Furthermore, they contribute to reducing biochar production and facilitate its decomposition into hydrocarbons and for supporting the circular carbon economy [15–18]. Various catalysts have been used in this regard, which can be categorized into molecular sieve catalysts (such as ZSM-5, Y-type, Beta type, MCM-41, SBA-15, micro mesoporous composite molecular sieve), alkali metal-base catalysts (alkaline earth metal oxides and alkali metal salt), and transition metal based catalyst (including nickel, zinc, copper, iron, cobalt, manganese), all of which demonstrate significant potential in this field. The upgrading process is facilitated by the porous structure and high acidity of the catalysts, their morphological selectivity, thermal stability, and commercial availability [19,20]. However, these catalysts are characterized by a rigid structure, fixed acidity, and limited structural flexibility, leading to strong hydrocarbon adsorption within their microporous framework, thus clogging the pores and disabling the catalyst [21,22]. This necessitates the development of new, flexible catalysts capable of overcoming these limitations. In this context, metal-organic frameworks (MOFs) have recently been introduced as advanced catalysts for catalytic pyrolysis due to their unique flexible structure, large surface area and porosity, precise pore size, and leading catalytic capabilities [23]. In addition to their high selectivity and strong acidic and metal centres, which provide better control over the selectivity of chemical compounds, they enhance surface interactions during the pyrolysis process [24,25]. MOFs have already been used with different types of biomass, such as sawdust (at 600 °C and 800 °C for sustainable hydrogen production using Ni-MOF and Ce-Ni-MOF catalysts) [26], tobacco straw (400-550 °C using ZIF-67/ZSM-5 catalyst) [27], waste wood (for high-quality bio-oil production using Ni-MOFs and Mg-MOFs at 450 °C - 600 °C) [28], chlorella vulgaris for high aromatic hydrocarbons in bio-oil (using Ni-Cu@C, Ni-Co@C, Cu-Co@C and Ni-Cu-Co@C at 600 °C) [29], sewage sludge using microwave pyrolysis (using modified MIL-100(Fe) at 400 °C, 500 °C, or 600 °C) [30], efficiently converting soybean oil into biodiesel over Cr-ZIFs-8/ZnCo-LDH [31], bamboo modified MIL-101(Cr) at 600 - 800 °C using microwave-assisted catalytic pyrolysis to produce MAH-rich bio-oil [32]. Despite the promising results, most of these studies attribute the emitted hydrocarbons exclusively to the decomposition of biomass, ignoring the contribution of the degradation of MOF linkers, which decompose at a lower temperature (<450°C) than that of the biomass (520 °C), directly contributing to the formation of the observed liquid products and increasing their productivity as demonstrated by our group using TAG and FTIR [33]. This misinterpretation obscures the true catalytic role of MOFs and highlights a fundamental limitation: their low thermal stability, which is below the decomposition temperatures required for biomass. Consequently, this intrinsic instability not only compromises catalytic performance but also challenges the reliability and scalability of MOFs in feverish temperature catalytic co-pyrolysis processes.

To overcome the limited thermal stability of many previously reported MOFs, recent research has focused on the development of more thermally robust framework materials. Among the thousands of MOFs reported to date, zeolite imidazole framework-67 (ZIF-67) has attracted considerable attention because of its excellent thermal stability, high specific surface area, and well-defined cobalt-based active sites. Biomass pyrolysis is typically conducted within the temperature range of 300-600 °C, where increasing temperature accelerates biomass decomposition, enhances secondary cracking and deoxygenation reactions, and strongly influences the composition of the evolved vapors. Therefore, the catalyst must remain structurally stable throughout this temperature ranges to sustain its catalytic activity. Our previous study demonstrated that ZIF-67 maintains its crystalline structure up to 600 °C, making it suitable for biomass pyrolysis [34], which is typically conducted within this temperature range. This thermal stability enables ZIF-67 to withstand the operating temperatures employed in the present study, allowing its porous structure and cobalt active sites to effectively promote carking and aromatization reactions during biomass pyrolysis [35,36]. Moreover, recent environmental and techno-economic assessments have highlighted the potential of ZIF-67 for large-scale applications [37,38]. To explores the potential of ZIF-67 as a novel and versatile catalyst for upgrading biomass pyrolysis products, this research aims to study the pyrolysis behaviour of woody biomass in the presence of ZIF-67 using a combination of analytical micro-scale reactor experiments and modelling techniques. The thermal decomposition behaviour of biomass was investigated using thermogravimetric (TG) analyser at various heating rates and ZIF-67 catalyst loadings (10, 20, and 30 wt%). The influence of ZIF-67 content on the composition of the evolved catalytic vapors was evaluated using TG-Fourier transform infrared (TG-FTIR) spectroscopy and gas chromatography-mass spectrometry (GC-MS). These analyses enabled the identification of the optimal catalyst loading for enhancing the decomposition rate and increasing the yield of aromatic compounds in the released vapors. Furthermore, the effect of ZIF-67 on the pyrolysis kinetics of biomass was assessed using several models, including Kissinger-Akihira-Sonoze (KAS), Flynn-Wall-Ozawa (FWO), and Friedman (FM), and Vyazovkin (VN) approaches. The corresponding thermodynamic parameters were subsequently determined to provide further insight into the catalytic pyrolysis process. Finally, an artificial neural networks (ANN) model was developed and trained to predict the pyrolysis behaviour of biomass over ZIF-67, enabling the estimation of decomposition characterises under previously unexamined operating conditions.

2. Experimental and methodology

2.1. Materials and its characteristics

ZIF-67 (cobalt-based 2-methylimidazole framework, molecular weight 221 g/mol) was purchased from PlasmaChem© company. The structural, physical, and chemical properties of ZIF-67 have been reported in the literature, including X-ray diffraction patterns, BET surface area, SEM morphology, and pore properties [35]. Wood pellets (WP) were used as the woody biomass feedstock in the present research and were obtained from a local supplier in Lithuania. According to the supplier's specifications, the pellets has diameter of 6 mm, length of 3.15-40 mm, dust particles of ≤0.5%, bulk density of 600-750 kg/m^3, calorific value of 4.6 kWh/kg, sulfur content of ≤0.04%, and chlorine content of ≤0.02 wt%. Also, the WP sample was characterized by elemental and proximate analyses and the elemental composition was determined using a CHNS elemental analyser, while the oxygen content was calculated by difference. Proximate analysis was performed using a Netzsch STA 449 F3 Jupiter thermogravimetric analyser in accordance with ISO 18123:2023, ISO 18122:2022, and EN 14774–1:2009 standards. The WP sample consisted of 49.20 wt% carbon, 5.68 wt% hydrogen, 0.18 wt% nitrogen, 44.94 wt% oxygen. The proximate

analysis revealed 9.78% moisture, 74.82% volatile matter, 14.69% fixed carbon, and 0.71% ash. Before catalyst mixing, the WP was first ground using an electric grinder subsequently sieved to obtain particles smaller than 200 μm. The resulting WP powder was then mixed with ZIF-67 at catalyst loadings of 10, 20, 30 wt% using an electric grinder operated at the lowest speed for 5 min to ensure homogeneous mixing while minimizing potential damage to the ZIF crystal structure. The prepared mixtures were designated as ZIF/WP10, ZIF/WP20, and ZIF/WP30 according to their respective catalyst contents. These mixtures were used to evaluate the effect of ZIF-67 loading on WP pyrolysis behaviour and to identify ZIF-67-to-WP ratio for maximizing the production of aromatic compounds in the evolved pyrolysis vapors. A flowchart illustrating the experimental methodology for the analysis of ZIF/WP pyrolysis is presented in Fig. (1), while detailed descriptions of each stage are provided in the following sections.

2.2. Thermogravimetric analysis

The effect ZIF-67 and its content on the thermal decomposition of WP was monitored using a TGA device (NETZSCH model, Selb, Germany), which served as an analytical-scale pyrolysis reactor. The TGA measurements were conducted under a nitrogen atmosphere with a gas flow rate of 60 mL/min. For each experiment, the total sample mass, including both biomass and ZIF-67 catalyst (10, 20, or 30 wt%), was maintained at approximately 10 mg. To minimize mass and heat transfer limitations, a small sample mass (~10 mg), a uniform biomass catalyst mixture, and an open alumina crucible. The thermal decomposition behaviour of WP and ZIF/WP samples was investigated at heating rates of 10, 20, and 30 °C/min, which are standard conditions for TGA kinetic studies. These various heating rates also are needed for molding the pyrolysis kinetics of ZIF/WP and studied its effect on the yield and chemical composition of the evolved vapors resulted from the pyrolysis process. Reproducibility was confirmed by repeating TGA measurements of WP sample three times at lower heating rate (10 C/min), resulting in highly consistent data with minimal deviation. The weight loss of WP and ZIF/WP samples were monitored in the progress of temperature under the controlled heating rates to generate TGA curves. Derivative thermogravimetric (DTG) curves of the samples were subsequently obtained by numerical differentiation of the measured TGA data via Proteus software. Finally, the conversion efficiency of ZIF/WP samples was quantified using the thermal decomposition index (CPI), as expressed in Eq. [1] [39].

$$\mathrm{CPI} = \frac{(-R_{\max}) \times (-R_{\mathrm{avg}}) \times M_{\mathrm{f}}}{T_{int} \times T_{peak} \times \Delta T_{1/2}} \quad (1)$$

where R_{max} (% min^{-1}), R_{avg} (% min^{-1}), M_f (%), T_{int} (°C), T_m (°C), and $\Delta T_{1/2}$ (°C) parameters are defined as maximum partial decomposition rate, average mass loss rate, final mass loss, initial evaporation temperature, maximum decomposition temperature, and half-peak temperature with at $R/R_{peak} = 0.5$, respectively.

2.3. Pyrolysis vapor analysis

Volatile species released from the decomposition of WP and ZIF/WP samples in the principal decomposition region were characterized by TG-FTIR and GC/MS. TG-FTIR (Bruker Tensor 27, Germany) was used to identify the functional groups of the volatile species evolved from the pyrolysis of ZIF/WP samples. The vapor species evolved during TGA were transferred directly to the FTIR via an infrared gas cell equipped with a potassium bromide as an inner window and a zinc selenide as an outer window. Infrared spectra were collected over the range of 700 to 4400 cm^1 using a liquid-nitrogen cooled mercury-cadmium-telluride detector, averaging 32 scans per spectrum. Whereas, identification of the pyrolysis vapor and their relative abundances was performed using GC/MS (Agilent 7890A GC coupled to a 5975 MSD) with helium (purity >99.9999%) as the carrier gas, operating at 20 psi and 250°C. Vapors released from the quartz tube were introduced into a GC/MS system and separated on HP-5MS ((5%-phenyl)-methylpolysiloxane) column. Column dimensions were 60 m (length) × 250 μm (inner diameter), 0.25 μm film thickness. The oven temperate was programmed from 40 °C to 270°C and 10 °C/min as a heating rate. Mass spectra of the evolved volatile species from the decomposition of ZIF/WP samples were recorded over an *m/z* range of 30-600 via electron ionization. The pyrolysis species were identified by comparing their mass spectra with those contained in the National Institute of Standards and Technology (NIST) Mass Spectral Library, together with their corresponding retention times. Since the objective of the GC-MS analysis was the identification and relative comparison of the evolved products, authentic calibration standards were not employed. Therefore, the reported values represent relative GC-MS chromatographic peak area parentages, obtained by automatic integration using the Agilent GC-MS data processing software, and should be regarded as semi-quantitative indicators of the relative abundance of the identified compounds rather than absolute

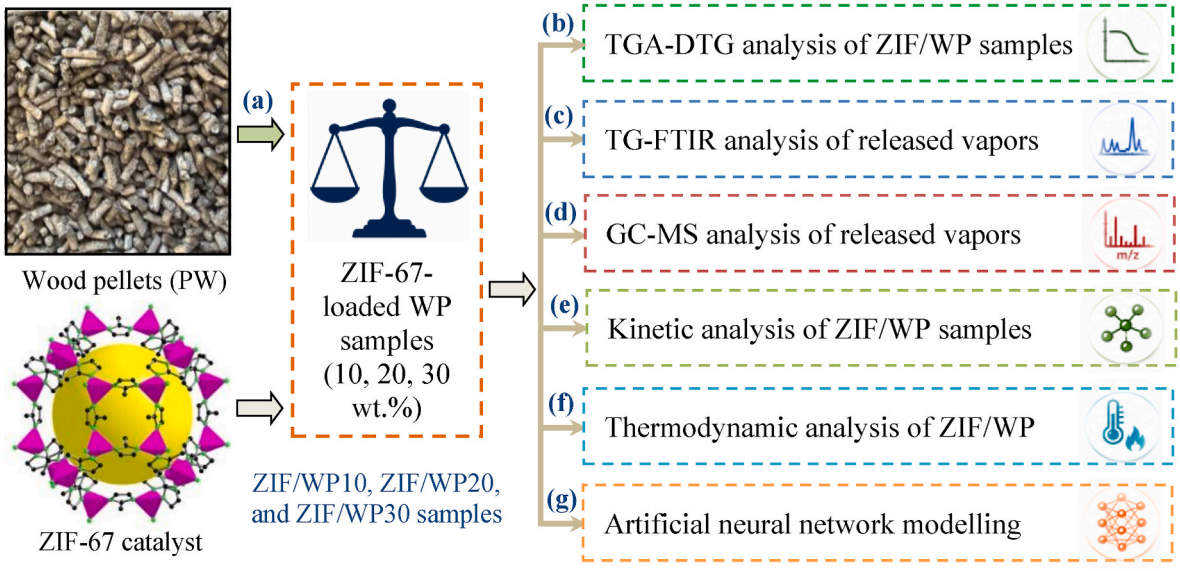

Figure (1). Flowchart of the experimental methodology for biomass pyrolysis over ZIF-67.

product yields or concentrations. Baseline correction, peak deconvolution, and peak integration were performed automatically using the GC-MS data processing software. For partially overlapping chromatographic peaks, the extracted mass spectra at the peak apex and across the peak profile were carefully inspected, and compound identities were verified through comparison with the NIST mass spectral library. Only compounds exhibited reliable spectral matching and adequate chromatographic resolution were included in the reported results.

2.4. Kinetic modelling

The catalytic pyrolysis kinetic of WP and ZIF/WP samples was modelled using KAS, FWO, and FM as a most common linear kinetic approach model-free linear isoconversional methods. These approaches are valued due to their simplicity as they analyse single-step reaction behaviour without requiring assumptions about the reaction mechanism or kinetic orders [40]. Also, the VN model was employed the present research as a common nonlinear kinetic approach for studying the catalytic pyrolysis kinetic of ZIF/WP samples. This approach assumes that the biomass consists of several sub-components and they decomposed in parallel under the applied temperature. The final formulas of the selected models are defined as in Eqs. [2–5] [41]. This diversity in the selected models lead to choose the situatable model that can be used for estimating the catalytic pyrolysis kinetic of ZIF/WP samples in terms of activation energy (Ea) with high correlation coefficient (R^2) (Eq. [6] [42]) value to describe the complex reaction mechanism of ZIF/WP samples. Also, the pre-exponential factor (A) was calculated that needed for determining the thermodynamic parameters later.

$$\textbf{KAS}: \ln\left(\frac{\beta}{T^2}\right) = \ln\left(\frac{AR}{Eag(y)}\right) - \frac{-Ea}{RT} \tag{2}$$

$$\textbf{FWO}: \ln\beta = \left(\frac{\ln AEa}{Rgy}\right) - 5.335 - \frac{1.0516Ea}{RT} \tag{3}$$

$$\textbf{FM}: \ln\left(\frac{\beta dy}{dT}\right) = \ln(Af(y))\left(\frac{-Ea}{RT}\right) \tag{4}$$

$$\textbf{VZ}: (y) = \int_0^{\alpha} \frac{dy}{f(y)} = A\int_0^{t} \exp(-E/RT)dt \tag{5}$$

$$R2 = 1 - \sum_{i=1}^{N}\left(H_i - H_{i,mol}\right)^2 \Big/ \sum_{i=1}^{N}\left(H_i - H_{i,avg}\right)^2 \tag{6}$$

2.5. Thermodynamics analysis

The effects of ZIF-67 addition at different ratios on thermodynamic parameters of WP pyrolysis were investigated. These parameters, namely enthalpy (ΔH: kJ/mol), Gibbs free energy (ΔG: kJ/mol), and entropy (ΔS: kJ/(mol K)), were calculated using expressions presented in Eqs. [7–9] [43]. Ea (kJ/mol) and A (s^{-1}) parameters were obtained from kinetic analysis at each conversion level using KAS, FWO, and FM approaches. While the constants K_B and h represent the Boltzmann constant (1.3819×10^{-23} J/K) and Planck constant (6.626×10^{-34} J s), respectively [44].

$$\Delta H = Ea - R(T_m) \tag{7}$$

$$\Delta G = Ea + RT_m \ln\left(\frac{K_B T_m}{hA}\right) \tag{8}$$

$$\Delta S = \frac{\Delta H - \Delta G}{T_m} \tag{9}$$

2.6. Artificial neural network modelling

The developed ANN models were designed exclusively to predict the thermal decomposition behavior (TGA profiles) of WP and ZIF-67/WP samples using TGA data as the training dataset. The thermal decomposition of WP and ZIF/WP samples at an unknown heating rate were predicted using an ANN approach as an effective methodology for nonlinear patterns even in the presence of noisy data through advanced training and validated algorithms [45]. The ANN algorithm was developed using MATLAB and implemented through sequential phases of network construction, training, validation, and testing. In this work, separate ANN models were developed for each investigated sample (WP, ZIF/WP10, ZIF/WP20, and ZIF/WP30). Each model was trained using TGA datasets generated at different heating rates to predict the corresponding thermal decomposition in terms of mass loss profiles. Therefore, catalyst loading was treated as a fixed characteristic of each dataset rather than as an independent input variable. The architecture of the suggested ANN comprises three principal layers distributed by the following way: an input layer including the decomposition temperature and heating rate; a hidden layer for data processing; and an output layer that responsible for showing the predicted TGA data under unknown degradation performance. The developed network was trained via the Levenberg-Marquardt (LM) backpropagation methodology that selected due to its fast convergence and high capability in simulating nonlinear systems [46]. A nonlinear activation function was applied within the hidden layer and adjusted iteratively based on trial-and-error principle to increase R^2 value that described in Eq. [6]. The dataset was randomly divided into subsets distributed as follows: training (70%), validation (15%), and testing (15%). These percentages were chosen based on findings in the literature, which showed that this split provides a well-balanced framework for model learning, hyperparameter adjustment, and performance assessments, especially in the case of medium to large sized datasets [47]. The performance of the developed network was assessed based on R^2, mean absolute error (MAE), mean bias error (MBE), and Root means square error (RMSE), which can be expressed as in **Eqs.** [6,10–12] [48,49]. The number of neurons in the hidden layer was varied between 3 and 10, and each network configuration was evaluated based on MSE and R^2 metrics. Among the tested models, the network with 3 × 3 × 1 architecture achieved the lowest validation error. Hyperparameter optimization process was carried out automatically based on the LM methodology, which adaptively updates the learning rate throughout the training process. The maximum number of epochs was specified to allow the model convergence, while early stopping based on validation performance was applied to avoid extra training. Prior to training, all input and output parameters were scaled to the range [0,1] through minimum and maximum normalization. The normalization factors were extracted from the training dataset and subsequently applied to the datasets. Lasty, the refined ANN model was applied to predict the TGA data of ZIF/WP samples with different content of ZIF at 25 °C/min, a regime that was not directly examined experimentally using TGA instrument.

$$MAE = \frac{1}{N}\sum_{i=1}^{N}\left|H_i - H_{i,mol}\right| \tag{10}$$

$$MBE = \frac{1}{N}\sum_{i=1}^{N}\left(H_i - H_{i,mol}\right) \tag{11}$$

$$RMSE = \sqrt{\frac{1}{N}\sum_{i=1}^{N}\left(H_i - H_{i,mol}\right)^2} \tag{12}$$

3. Results and discussion

3.1. Thermogravimetric analysis of ZIF/WP samples

Fig. 2 presents the TGA and DTG curves of WP and ZIF/WP samples obtained the different heating parameters (10, 20, 30 °C/min). The TGA profile of WP sample (Fig. (2A)) exhibited three main decomposition regions (W1-W3), with an overall weight loss ranging from 77 to 86 wt% depending on the heating rate. In the first region (W1), a minor weight

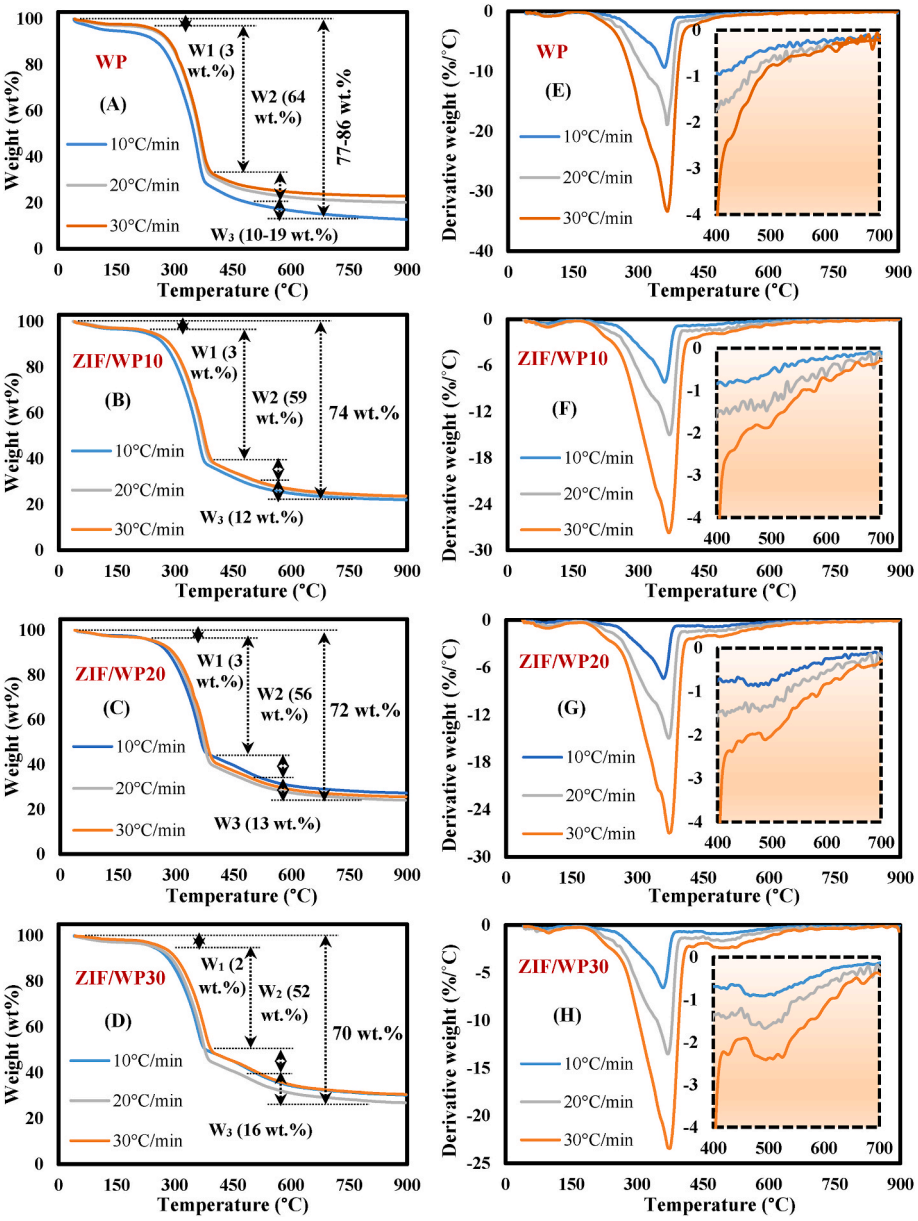

Figure (2). A-D) TGA and E-H) DTG curves of WP and ZIF/WP samples.

loss (<3 wt%) was observed up to 140 °C, which was attributed to release the moisture content of the supplied WP. In the second region (W2), substantial decomposition occurred, resulting in approximately 64 wt% weight loss up to 400 °C due to the decomposition of hemicellulose and cellulose components [50,51]. In the third region (W3), a gradual weight loss of 12-19 wt% was observed (≤600 °C) indicates the decomposition of lignin subcomponent that exhibits higher thermal stability and decomposes over a broader temperature range than hemicellulose and cellulose. However, the significant mass loss occurring between 250 and 520 °C, and the slight decomposition observed above this range, are associated with gradual carbonization and secondary cracking reactions for biochar formation in the last stage [52]. In case of ZIF/WP samples (Fig. (2B-D)), the TGA curves exhibited decomposition profiles similar to those of the neat PW sample, consisting of three successive decomposition zones. The first stage corresponding to moisture evaporation, resulting in a weight loss of 2-3 wt% up to 140 °C. Subsequently decomposition hemicellulose and cellulose content up to 400 °C, but with different weigh loss values, in particular 59% (ZIF/WP10), 56% (ZIF/WP20), and 49% (ZIF/WP20). Then the process ended by decomposition of lignin subcomponent in the range of 400-600 °C with loss of 12-16 wt%, followed by the solid formation zone. This decomposition zone also includes the release of residual organic species from ZIF-67 organic linker, which decompose at elevated temperatures [34]. As displayed, the ZIF/WP samples decomposed completely up to 600 °C with overall weight loss estimated at 74% (ZIF/WP10), 72% (ZIF/WP20), and 70% (ZIF/WP20). However, the high char yield in case of ZIF/WP samples can be attributed to the presence of metal nodes, which possess high thermal stability and melting point [53], thereby promoting the formation and retention of solid carbonaceous products. While the DTG curves of WP and ZIF/WP samples (Fig. (2E-H)) exhibited a dominant decomposition peak, with the corresponding peak decomposition temperatures ($\mathbf{T_m}$) ranging from 360 to 368 °C (WP), 359-371 °C (ZIF/WP10), 359-371 °C (ZIF/WP20), and 359-375 °C (ZIF/WP30). The presence of a single major DTG peak suggests that the decomposition of the ZIF-67 organic linker overlapped with the degradation of WP components, resulting in a merged decomposition peak. Finally, the catalytic pyrolysis behaviour of WP and ZIF/WP samples at the specified heating rates was estimated based on

the measured TGA and DTG data, and the resulting characteristics parameters are summarized in Table 1.

3.2. TG-FTIR analysis of pyrolytic vapors

The pyrolytic vapors evolved during the principal decomposition stage of WP and ZIF/WP samples at the listed heating rates were characterized using TG-FTIR analysis. The corresponding two-dimensional FTIR (2D-FTIR) and three-dimensional FTIR (3D-FTIR) spectra, which the functional groups present in the released vapors, are shown in Fig. 3. The 2D-FTIR spectrum of the WP sample exhibited two prominent absorption bands at 1735 cm^{-1} and 2362 cm^{-1}, which were assigned to C=O stretching vibration of carbonyl groups and the asymmetric stretching vibration of CO_2, respectively. In addition to these dominant peaks, several weaker absorption bands were observed at 1093 cm^{-1} (C-O stretching in alcohols, ethers, carboxylic acids, and esters compounds), 1392-1513 cm^{-1} (C-H stretching), 2800-2950 cm^{-1} (alkyl C-H stretching region), and 3580-3860 cm^{-1} (O-H stretching). These spectra features are consistent with those reported for pyrolysis vapors generated from woody biomass in the previous studies [46]. In the case of ZIF/WP samples, the 2D-FTIR spectra exhibited absorption bands at similar wavenumbers and with comparable spectrum to those observed from the neat WP sample. This observation indicates that the volatile products detected during the principle decomposition stage originated predominantly from the thermal degradation of the WP. It should be noted that the TG-FTIR spectra were collected at the maximum decomposition region of the DTG curves, corresponding to 359-375 °C (Table 1), whereas our previous study demonstrated that pure ZIF-67 undergoes its main thermal decomposition between 569 and 607 °C [34]. Therefore, under the experimental conditions employed for TG-FTIR analysis, ZIF-67 remained thermally stable and did not produce detectable volatile decomposition products. Consequently, no additional FTIR absorption bands associated with the decomposition of the ZIF-67 organic linker were observed. Nevertheless, although ZIF-67 did not to directly contribute volatile species within this temperature range, its catalytic active sites may have influenced the reaction pathways of biomass pyrolysis, and consequently the composition of the evolved vapors. The corresponding 3D-FTIR spectra further confirmed the evolution of multiple gaseous products during the thermal decomposition of bot WP and ZIF/WP samples at the investigated heating rates. The similarity of the spectral profiles indicates that the major functional groups released during pyrolysis remained unchanged, while any catalytic effect of ZIF-67 is more likely reflected in the relative abundance of individual volatile compounds, as discussed in the subsequent GC-MS analysis. Finally, the intensity of the absorption bands increased with rising heating rate, indicating increased vapor emission resulting from thermal decomposition. This is attributed to the fact that a higher heating rate enhances heat flux within the biomass matrix, accelerating the decomposition of their sub-components and promoting the formation and evolution of volatile compounds [54].

3.3. GC/MS analysis of pyrolytic vapors

GC/MS analysis was employed to characterize the pyrolytic vapors evolved from WP and ZIF/WP samples at different heating rates. The analysis was conducted withing the principal decomposition region determined from the DTG profiles, allowing the effect of ZIF-67 addition on the composition and distribution of the resulting pyrolytic vapors to be assessed. Fig. 4 presents the GC/MS chromatogram of WP vapors, while the identified compounds and their corresponding relative peak areas are summarized in Table 2. As shown, the GC-MS analysis revealed that the pyrolysis of WP consisted of a complex mixture of oxygenated organic compounds, including aldehydes, ketones, alcohols, furans, and phenolic derivatives. At all heating rates, oxygenated compounds predominated with pentanal (29.56%) and cyclohexanol, 5-methyl-2-(1-methylethyl)-, acetate (25.93%) being the major compounds at 10 °C/min, while phenolic compounds, particularly phenol, 2-methoxy-4 methyl- (25.57-33.86%), became dominant at higher heating rates. The increase in heating rate also promoted the formation of ketones, such as 2-cyclopenten-1-one, 3,4,4-trimethyl- (30.28%), indicating enhanced thermal cracking and secondary reactions. These results demonstrate that WP pyrolysis primarily generates oxygen-rich volatile compounds originating from the decomposition of WP components, with product distribution strongly influenced by the heating rate and these results are in good agreement with the reported biomass pyrolysis results in the literature [55]. Fig. 5 presents the GC/MS chromatogram of ZIF/WP20 vapors, while the GC/MS spectrums of ZIF/WP10 and ZIF/WP30 samples are provided in the Supplementary Materials (Figs. (S1, S2)). The chemical compounds identified in the vapors of all ZIF/WP samples, along with their relative peak areas are listed in Table 3. According to the GC-MS analysis, the predominant aromatic product generated during the catalytic pyrolysis was naphthalene, 1,2,3, 4 tetrahydro-2-phenyl- ($C_{16}H_{16}$), representing approximately 62.8-84.7% of the total identified GC peak area, depending on the ZIF-67 loading and heating rate. In addition to C16H16, several aromatic compounds were detected in relatively low abundance, including benzene, 1,1'-(3-methyl-1-propene-1,3-diyl)bis- (6.4-7.1%), 2, 5-Diphenyl-1,5-hexadiene (2.7-5%), alpha-phenyl-alpha tropylacetaldehyde tosylhydrazone (3.2-7.3%), etc. Conversely, the conventional BTX compounds (benzene, toluene, ethylbenzene, and xylenes) were not detected as major products. Thes findings indicate that ZIF-67 was not specifically directing the pyrolysis toward the selective production of $C_{16}H_{16}$. Rather, it promoted the formation of aromatic hydrocarbons, with $C_{16}H_{16}$ begging the dominant aromatic compound under the applied catalytic pyrolysis conditions. The relative abundance of $C_{16}H_{16}$ ranged from 73.01 to 79.21% (ZIF/WP10), 62.81-84.65% (ZIF/WP20), and 66.45-75.95% (ZIF/WP30). The highest relative abundance of $C_{16}H_{16}$ compound was obtained for the ZIF/WP20 sample at 20 °C/min, accounting for approximately 84.7% of the total identified GC-MS chromatographic peak area as shown in Fig. (6). It should be emphasized that this value represent the relative chromatographic peak area of the identified compounds and should not be interpreted as an absolute product yields or mass concentrations. These results demonstrate the significant influence of ZIF-67 catalyst and its loading on the

Table 1
Pyrolysis characteristics of WP and ZIF/WP samples.

Sample	WP			ZIF/WP10			ZIF/WP20			ZIF/WP30		
Heating rate (°C/min)	10	20	30	10	20	30	10	20	30	10	20	30
$\mathbf{T_{int}}$ (°C)	247	215	198	173	178	184	148	173	189	156	175	187
$\mathbf{T_m}$ (°C)	360	368	368	359	371	370	359	371	371	359	371	375
$\mathbf{T_f}$ (°C)	451	474	505	673	677	678	683	689	693	686	689	691
$\mathbf{R_{max}}$ (%/min)	9.2	18.7	33.3	8.18	15	27.74	7.4	14.97	26.93	6.57	13.52	20.3
$\mathbf{R_{avg}}$ (%/min)	1.02	1.86	2.69	0.91	1.79	2.66	0.85	1.77	2.60	0.8	1.7	2.4
$\mathbf{M_f}$ (%)	12.78	20.25	22.98	22.0	23.4	23.8	27.27	24.07	30.2	30.2	26.8	30.5
ΔT1/2	59	69	83	63	80	88	62	78	78	64	78	91
CPI (%3 °C−3 min−2)	2.3E-05	1.3E-04	3.4E-04	4.2E-05	1.2E-04	2.9E-04	5.2E-05	1.3E-04	3.9E-04	4.4E-05	1.2E-04	2.3E-04

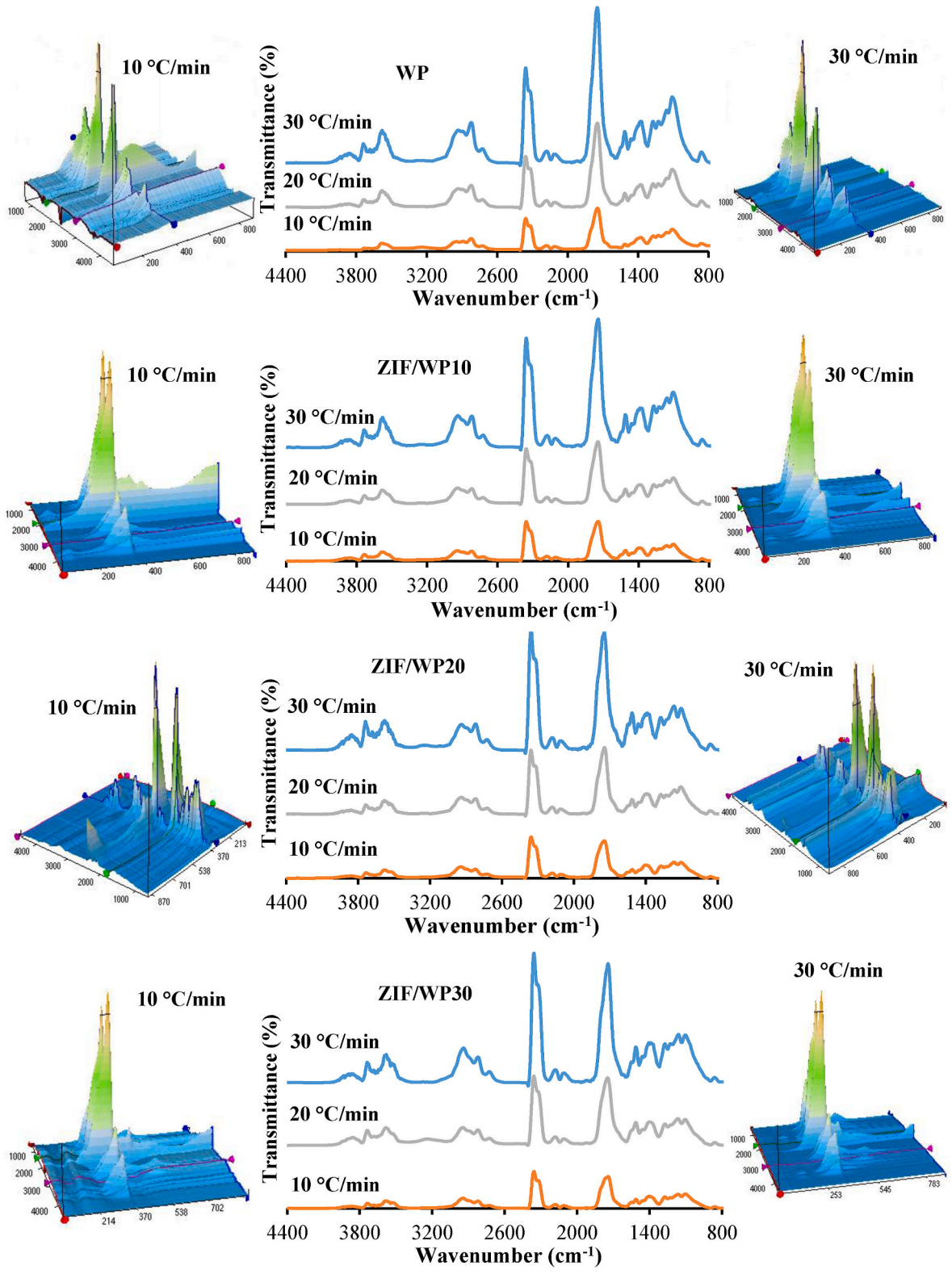

Figure (3). TG-FTIR (2D and 3D) of pyrolytic vapors evolved from WP and ZIF/WP samples.

composition of the generated biomass-derived vapors. The catalyst effectively promoted the deoxygenation and aromatization of pyrolysis intermediates, leading to the formation of vapor rich in aromatic hydrocarbons [56,57], in particular $C_{16}H_{16}$. This exceptionally high yield indicates that ZIF-67 possesses considerable potential for upgrading complex biomass vapor composition into valuable chemical products. The formation of $C_{16}H_{16}$ indicates an increase in aromatization during the upgrading process. As a phenyltetralin-type hydroaromatic compound, it represents a valuable class of aromatic hydrocarbon associated with a hydrogen donor source and potential applications in renewable fuel petrochemical feedstocks [58–62].

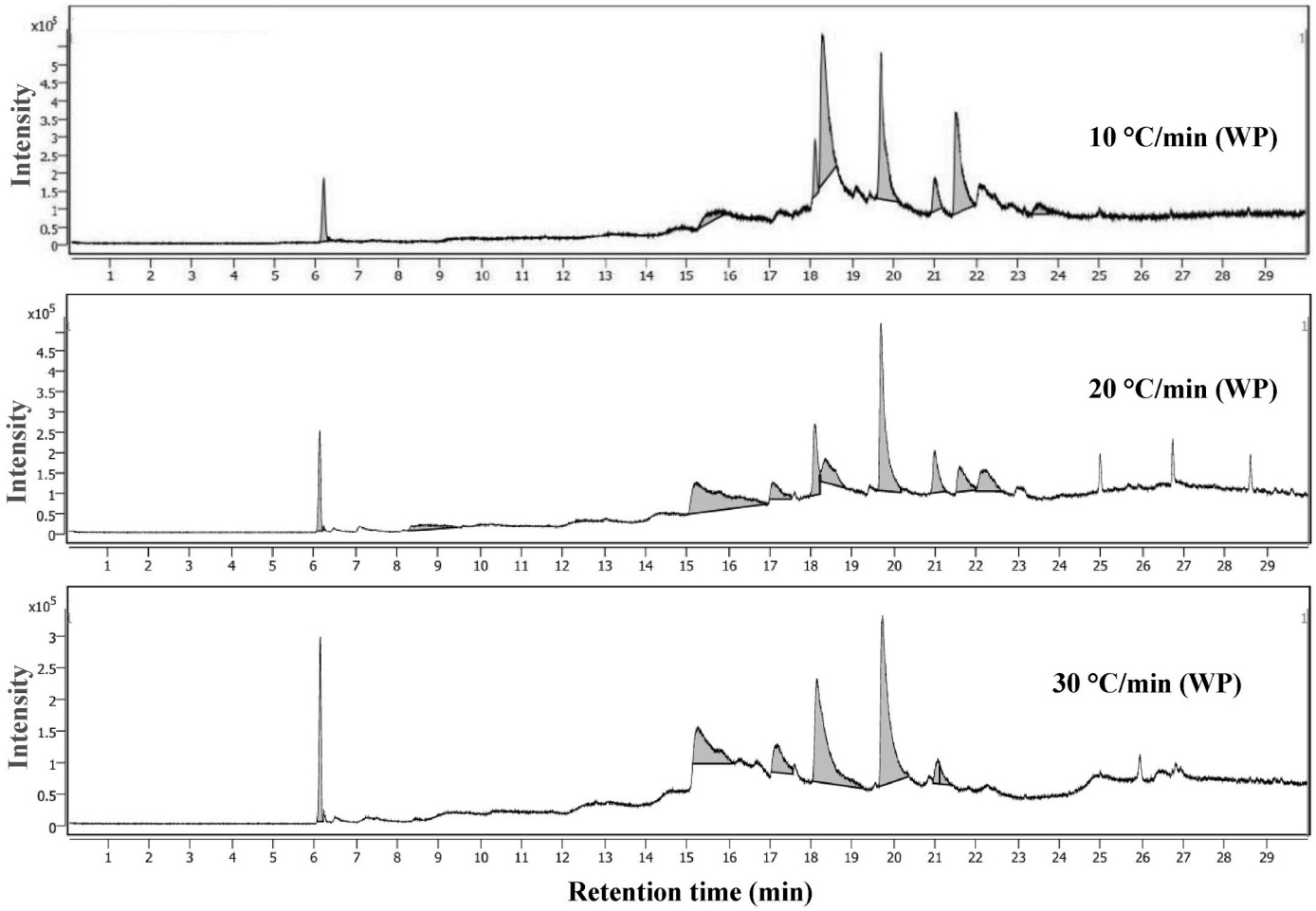

Figure (4). GC/MS spectrum of pyrolytic vapors of WP sample.

Table 2
GC/MS compounds of WP sample and their corresponding relative peak areas.

10°C/min			20°C/min			30°C/min		
Time (min)	GC Compound	Area (%)	Time (min)	GC Compound	Area (%)	Time (min)	GC Compound	Area (%)
6.190	l-Alanine ethylamide, (S)-	5.39	6.142	l-Alanine ethylamide, (S)-	5.36	6.139	l-Alanine ethylamide, (S)-	8.99
15.786	1,2-Cyclopentanedione	3.98	8.581	Hydrazine, ethyl-	3.75	15.272	1,2-Cyclopentanedione	15.06
18.105	2-Cyclopenten-1-one, 3,4,4-trimethyl-	4.50	15.234	1-(2 Tetrahydrofurylmethyl)pi peridine	25.28	17.187	2-Cyclopenten-1-one, 2 hydroxy-3-methyl-	7.46
18.279	Pentanal	29.56	17.071	2-Cyclopenten-1-one, 2 hydroxy-3-methyl-	4.44	18.139	2-Cyclopenten-1-one, 3,4,4-trimethyl-	30.28
19.687	Cyclohexanol, 5-methyl-2-(1-methylethyl)-, acetate	25.93	18.098	2-Cyclopenten-1-one, 3,4,4-trimethyl-	8.59	19.728	Phenol, 2-methoxy-4 methyl-	33.86
20.997	5-Isopropyl-3,3-dimethyl-2-methylene-2,3-dihydrofuran	4.79	18.357	2-Nonen-1-ol	7.68	21.068	4-Hydroxy-2,4,5 trimethyl-2,5 cyclohexadien-1-one	2.34
21.507	2-Methoxy-4-vinylphenol	22.84	19.680	Phenol, 2-methoxy-4 methyl	25.57	21.109	5-Isopropyl-3,3 dimethyl-2-methylene 2,3-dihydrofuran	2.01
23.514	3-Allyl-6-methoxyphenol	3.00	20.983	Phenol, 4-ethyl-2 methoxy-	6.07			
			21.605	Phenol, 3-methyl-5-(1 methylethyl)-, methylcarbamate	5.85			
			22.170	Cyclopenta[c]pentalen 3(3aH)-one, octahydro 1,2,3a,6-tetramethyl-	7.42			

3.4. Pyrolysis mechanism of ZIF/WP samples

During pyrolysis large scale, WP undergo thermal decomposition to generate volatile compounds, gases, and biochar. In case of using TGA as an analytical reactor, only pyrolysis vapors are produced (that can be observed its composition through GC-MS) combined with solid residue remaining at the end of reaction [63]. Since the present study is an analytical study and focused more fundamental pyrolysis of ZIF/WP

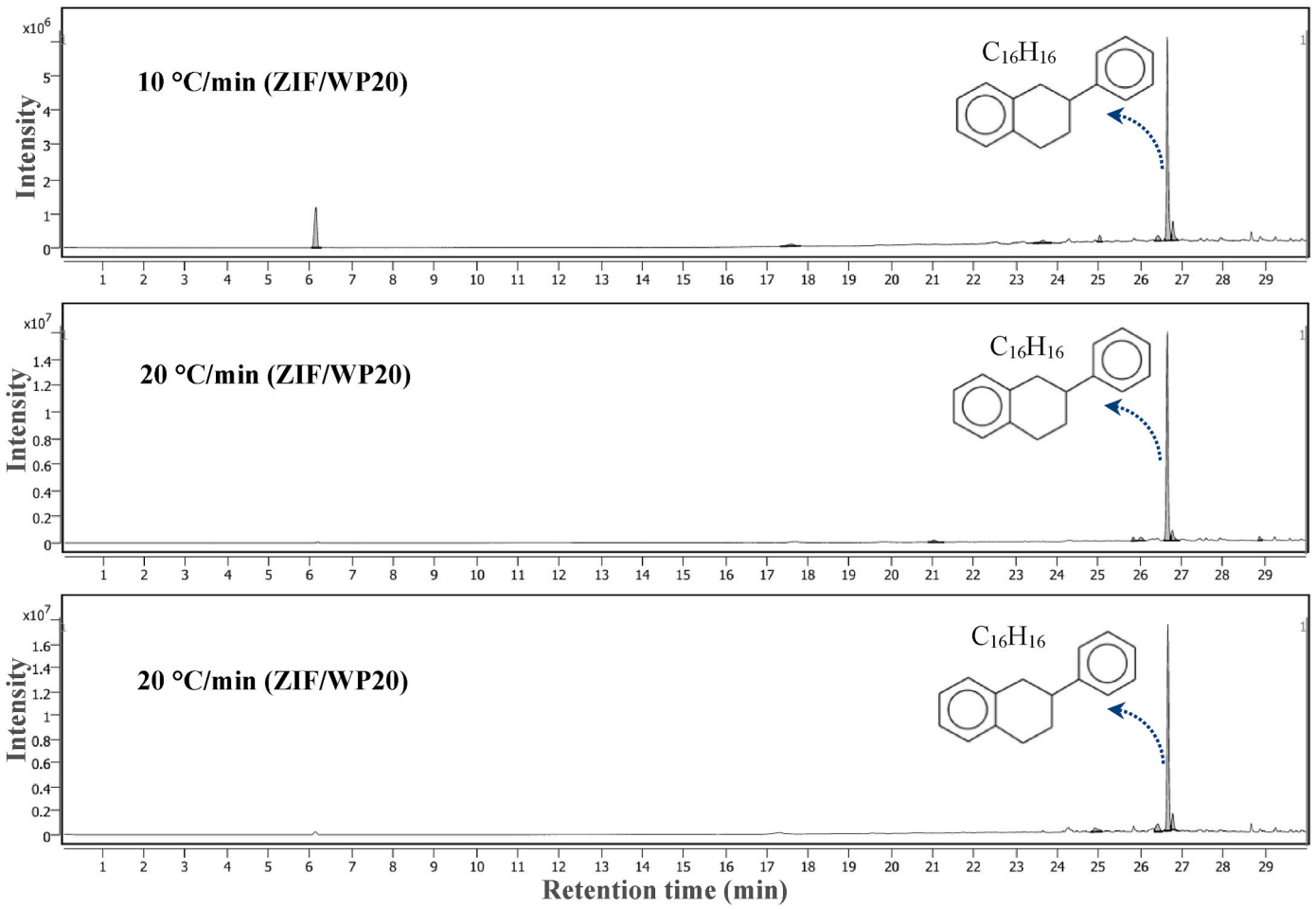

Figure (5). GC/MS spectrum of pyrolytic vapors of ZIF/WP20 sample.

samples, its pyrolysis mechanism was simplified and described based on the indicative TGA and GC-MS results of ZIF/WP20 sample that provide the higher $C_{16}H_{16}$ content, then compared with the decomposition features of neat WP and ZIF-67. The decomposition mechanism of all the specified samples at the same heating rate (20 °C/min) to ensure fair comparison and correct explanation as shown in Fig. (7). It should be noted that the thermal decomposition behavior of pure ZIF-67, including TGA and GC-MS analysis, has been thoroughly investigated and previously reported by our research group [34]. As displayed in the suggested pyrolysis mechanism, ZIF-67, WP, and ZIF/WP20 samples showed extremely low decomposition rate (<3w t.%) up to 140 °C due to release any moisture content (drying process). Another low decomposition rate (<3w t.%) was observed up to 260 °C for both WP and ZIF/WP20 samples due to the initiation of WP devolatilization and the breakdown of its main components, facilitating the release of light oxygenated compounds. As the temperature increased, hemicellulose decomposition occurred up to 320°C through deacetylation, depolymerization, decarboxylation, and dehydration reactions, producing volatile compounds like acetic acid, furfural, 2-furanmethanol, and CO_2 [64]. Subsequently, cellulose decomposition took place between 300 and 380°C, including glycosidic bond cleavage, transglycosylation, depolymerization, and fragmentation reactions to form levoglucosan and other oxygenated volatile species [65]. Whereas lignin decomposition continued over a much wider range of temperatures (250-900°C and the main primary decomposition occurred between 250 and 500°C through β-O-4 and α-O-4 bond cleavage, side chain scission, and demethoxylation reactions, generating phenolic compounds. At higher temperatures (>500°C), secondary pyrolysis reactions involving lignin-derived oligomers, heavy tar intermediates, and biochar became predominant [66]. Within this range, ZIF-67 sample showed a minor decompaction of less than 1 wt% due to evaporation of residual solvents and chemicals with higher boiling points and reaming in its porous structure. After that, the main activate decomposition zone of WP and ZIF/WP20 samples started to evaluate started by decomposition of hemicellulose content of WP (up to 300 °C), then cellulose (up to 400 °C), and lignin (up to 600 °C) [67]. While ZIF/WP20 sample showed features similar that obtained from decomposition of WP samples in all regions, but ZIF/WP20 sample showed a high solid reside content because of remaining ZIF-67 catalyst in this region without degradation. However, the vapor composition was completely different due to fact that the primary vapors synthesized from WP components underwent additional catalytic upgrading reactions, including deoxygenation, cracking, aromatization, alkylation, and cyclization, which promoted the conversion of oxygenated intermediates into aromatic hydrocarbons, as evidenced by the formation of $C_4H_6N_2$ compound detected by GC-MS analysis [68]. Where the present of ZIF-67 catalyst (ZIF/WP20), these compounds are adsorbed onto the ZIF-67 catalyst high surface area porous structure, and the active metal sites (cobalt) of ZIF-67 catalyst and its functional groups enhance the catalytic reactions and reduce the oxygen content of the vapors through deoxygenation and enhance the formation of aromatic hydrocarbons [69]. As previously mentioned, WP consists primarily of cellulose, hemicellulose, and lignin, which decompose within different thermal ranges. During thermal decomposition, the volatile products resulting from these biomass constituents are released sequentially and mixed before reacting with the ZIF-67 catalyst. Thus, the observed catalytic effects result from the

Table 3
GC/MS characteristics of ZIF/WP samples.

10°C/min			20°C/min			30°C/min		
Time (min)	GC Compound	Area (%)	Time (min)	GC Compound	Area (%)	Time (min)	GC Compound	Area (%)
ZIF/WP10 sample								
26.636	Naphthalene, 1,2,3,4 tetrahydro-2-phenyl-	78.45	21.500	Ethanone, 1-(2-hydroxy 5-methylphenyl)-	5.72	6.163	(2-Aziridinylethyl)amine	7.35
26.775	Alpha-phenyl-alpha tropylacetaldehyde tosylhydrazone	6.00	26.643	Naphthalene, 1,2,3,4 tetrahydro-2-phenyl-	79.21	13.636	1,6; 2,3-Dianhydro-4-O acetyl-. beta.-d allopyranose	4.21
28.231	1-Nonadecene	4.94	26.775	Alpha-phenyl-alpha tropylacetaldehyde tosylhydrazone	4.81	19.187	Benzoic acid	4.77
28.867	2,5-Diphenyl-1,5 hexadiene	5.01	28.231	Cyclopentane, 1-pentyl 2-propyl-	3.28	26.632	Naphthalene, 1,2,3,4 tetrahydro-2-phenyl-	73.01
29.629	Cyclodecane, octyl-	5.59	28.867	2,5-Diphenyl-1,5 hexadiene	3.67	26.768	Alpha-phenyl-alpha tropylacetaldehyde tosylhydrazone	7.26
			29.636	1,16-Hexadecanediol	3.31	26.979	E−15-Heptadecenal	3.40
ZIF/WP20 sample								
6.149	1,2 Hydrazinedicarboxamide	19.00	21.037	Heptasiloxane, 1,1,3,3,5,5,7,7,9,9,11,11 ,13,13-tetradecamethyl-	2.45	24.894	Heptasiloxane, 1,1,3,3,5,5,7,7,9,9,11,11 ,13,13-tetradecamethyl	4.27
17.581	Cyclododecanemethanol	3.05	25.836	Benzene, 1,1'-(1,3 propanediyl)bis-	1.91	26.415	Cyclododecanemethanol	6.35
23.666	Cyclohexane, 1,2,3,4,5,6-hexaethyl-	2.79	26.020	Octasiloxane, 1,1,3,3,5,5,7,7,9,9,11,11 ,13,13,15,15 Hexadecamethyl-	2.64	26.660	Naphthalene, 1,2,3,4 tetrahydro-2-phenyl-	82.24
25.024	Heptasiloxane, 1,1,3,3,5,5,7,7,9,9,11,11 ,13,13-tetradecamethyl-	2.52	26.656	Naphthalene, 1,2,3,4 tetrahydro-2-phenyl-	84.65	26.775	Benzene, 1,1'-(3-methyl 1-propene-1,3-diyl)bis-	7.14
26.422	Oxirane, 2-decyl-3-(5 methylhexyl)-, cis-(.+/ .)-	3.00	26.782	Benzene, 1,1'-(3-methyl 1-propene-1,3-diyl)bis-	6.43			
26.643	Naphthalene, 1,2,3,4 tetrahydro-2-phenyl-	62.81	28.881	Bicyclo[2.1.1]hexane, 1,4-diphenyl-	1.91			
26.779	Benzene, 1,1'-(3-methyl 1-propene-1,3-diyl)bis-	6.83						
ZIF/WP30 sample								
6.162	l-Alanine ethylamide, (S)-	4.42	6.162	l-Alanine ethylamide, (S)-	5.66	6.163	l-Alanine ethylamide, (S)	4.48
19.761	Phenol, 2-methoxy-4 methyl-	9.16	19.761	Phenol, 2-methoxy-4 methyl-	11.49	26.551	Cyclohexane, 1,3,5 triphenyl-	5.79
26.629	Naphthalene, 1,2,3,4 tetrahydro-2-phenyl-	75.84	26.629	Naphthalene, 1,2,3,4 tetrahydro-2-phenyl-	66.45	26.629	Naphthalene, 1,2,3,4 tetrahydro-2-phenyl-	75.95
26.779	Alpha-phenyl-alpha tropylacetaldehyde tosylhydrazone	3.18	26.779	Alpha-phenyl-alpha tropylacetaldehyde tosylhydrazone	5.56	26.775	Alpha-phenyl-alpha tropylacetaldehyde tosylhydrazone	5.11
28.864	2,5-Diphenyl-1,5 hexadiene	2.68	28.864	2,5-Diphenyl-1,5 hexadiene	4.80	28.231	1-Nonadecene	4.16
29.632	Heptane, 1,1 dicyclohexyl-	4.71	29.632	Heptane, 1,1 dicyclohexyl-	6.03	29.629	Cyclotetradecane	4.52

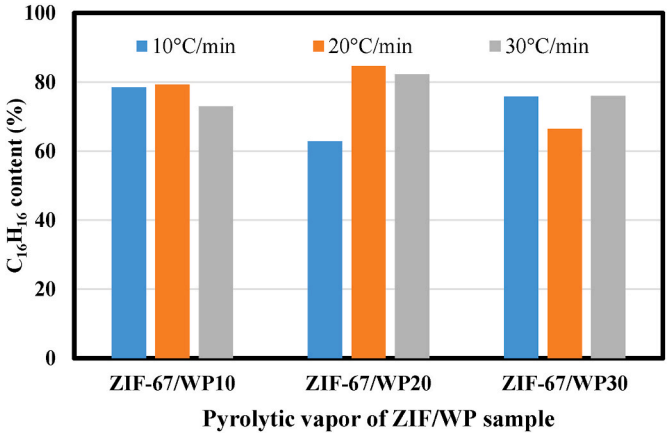

Figure (6). $C_{16}H_{16}$ content in the pyrolytic vapors of ZIF/WP samples.

co-conversion of the thermal decomposition vapors, and not solely from the selective conversion of the lignin-derived compounds. Ultimately, molecules with hard structure remained as solid residue aligned with ZIF-67 due to solid carbonaceous formation reaction [34]. Based on that, catalytic pyrolysis of biomass over ZIF-67 offers a promising approach for enhancing the economic value of biomass and upgrading their products.

3.5. Pyrolytic activation energy analysis

The impact of ZIF-67 catalyst with different concentration on the pyrolytic activation energy (Ea) of WP was estimated at various heating rates based on KAS, FWO, FM and the VN kinetic approaches. The Ea values of WP and ZIF/WP samples were calculated through fitting the relationship of each model then estimated the slope that is express as -Ea/R (KAS and Friedman) and −1.0516Ea/R (FWO) considered R = 8.31 JK^{-1} mol^{-1} [70]. The KAS, FWO and FM relationships with nine parallel linear paths (refers to energy at conversion rate in the range of 0.1-0.9) are shown in Fig. (8). It was noted that KAS and FWO relationships are provided a regular distribution of the conversion paths, especially at in the range of 0.2-0.9, where at the begging of reaction and lower conversion rate often several simultaneous reactions took a place making it difficult to simulate all its kinetics once. While in case in case of FM relationships, a large amount of randomness was observed due to the nature of this model that make it very sensitive to noisy data resulted

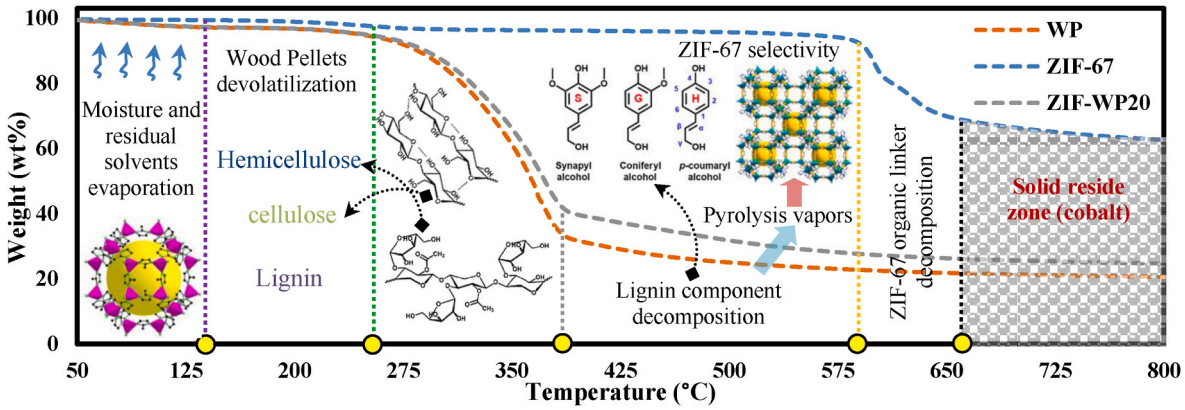

Figure (7). Pyrolysis mechanism of biomass over ZIF-67 catalyst.

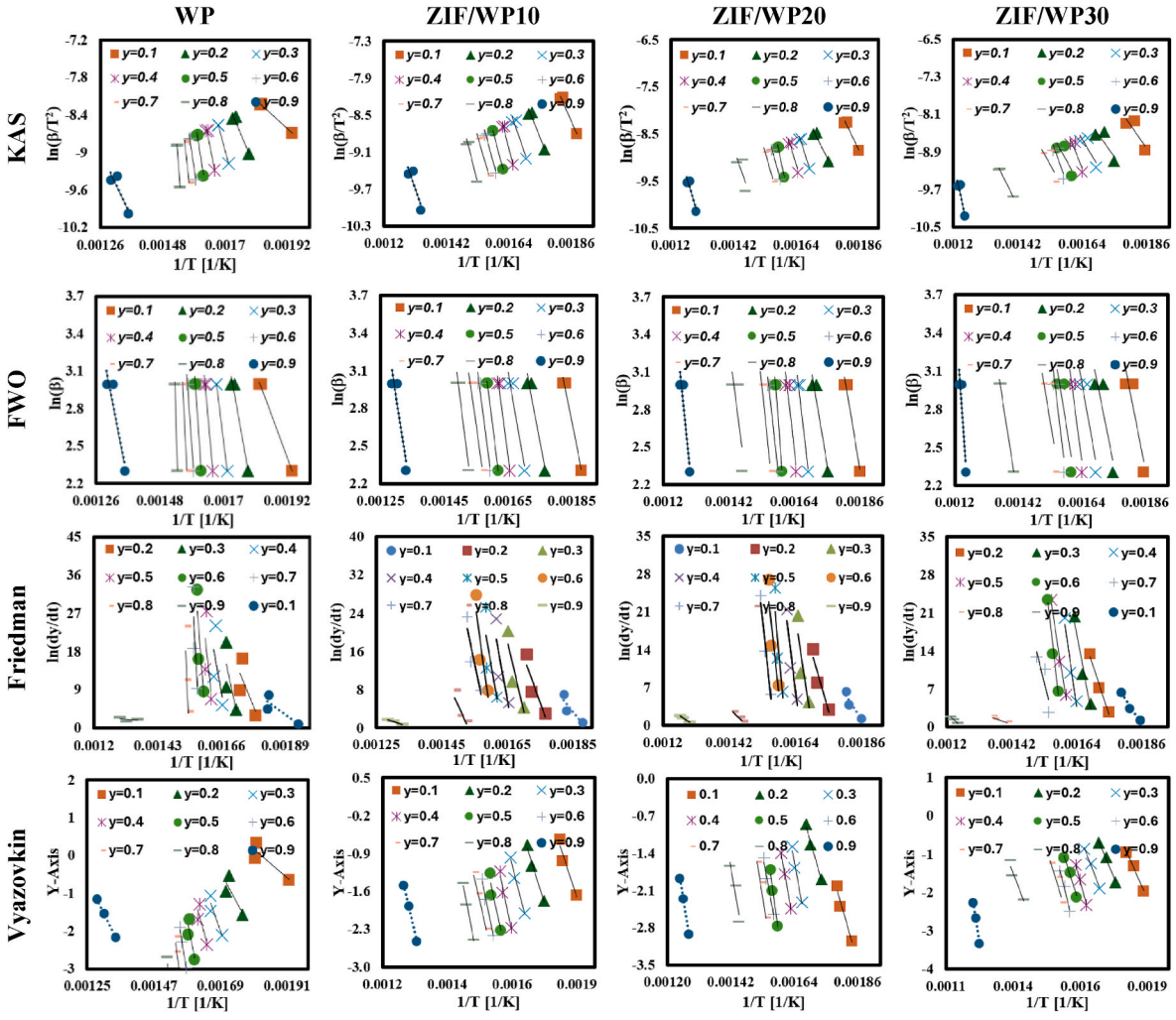

Figure (8). Fitting kinetics relationships of WP and ZIF/WP samples.

this randomness [71]. According to these relationships, the slops of each model was generated, then estimated the average values of Ea that ranging 233-427 kJ/mol (WP) with R^2 (0.878-0.970), 130-261.3 kJ/mol (ZIF/WP10) with R^2 (0.816-0.922), 159.3-295.3 kJ/mol (ZIF/WP20) with R^2 (0.882-0.917), and 120.5-251.6 kJ/mol (ZIF/WP30) with R^2 (0.838-0.959) as summarized in Table 4, while its Ea distribution as a function of conversion rate is presented in Fig. (9). As shown, the FM method exhibited greater fluctuations in the calculated Ea than the KAS and FWO methods. While the differential nature of the FM method makes it more sensitive to experimental uncertainties in DTG data, the observed variations are also likely associated with the complex multi-step mechanism of ZIF-67 catalysed biomass pyrolysis. The catalytic process involves overlapping primary and secondary reactions, including hemicellulose, cellulose, and lignin decomposition, catalyst-associated cracking, deoxygenation, aromatization, and char formation. These concurrent reactions can cause changes in the

Table 4
Activation energies of WP and ZIF/WP samples.

y	KAS			FWO			FM			VN	
	Ea (kJ/mol)	A (1/s)	R^2	Ea (kJ/mol)	A (1/s)	R^2	Ea (kJ/mol)	A (1/s)	R^2	Ea (kJ/mol)	R^2
WP sample											
0.1	35.0	2.7E+02	0.996	52.5	1.2E+08	0.998	43.7	8.1E+05	0.740	57.2	0.900
0.2	96.2	9.1E+05	0.957	113.7	1.8E+12	0.970	171.4	3.6E+13	0.750	121.5	0.910
0.3	144.3	2.0E+09	0.999	161.7	6.5E+15	1.000	253.5	5.8E+22	0.850	191.3	0.900
0.4	192.3	3.3E+12	0.947	209.8	3.0E+19	0.956	323.5	5.3E+27	0.888	327.2	0.990
0.5	271.0	7.0E+18	0.962	297.3	2.3E+25	0.967	498.4	2.7E+41	0.890	384.8	0.990
0.6	275.4	4.8E+18	0.943	296.4	5.8E+24	0.950	813.1	1.4E+65	0.920	478.4	0.985
0.7	384.7	2.3E+26	0.996	585.8	2.1E+33	0.997	786.9	4.9E+07	0.966	478.4	0.950
0.8	620.8	4.2E+43	0.998	638.2	1.4E+50	0.998	874.3	2.3E+12	0.997	785.9	0.900
0.9	78.7	2.5E+01	0.800	96.2	8.1E+07	0.900	78.7	1.4E+03	0.900	136.5	0.996
Avg.	233.1	4.7E+42	0.955	272.4	1.5E+49	0.970	427.0	1.6E+64	0.878	329.0	0.947
ZIF/WP10 sample											
0.1	87.4	6.0.E+06	0.972	113.7	5.3E+13	0.980	78.7	8.9E+08	0.800	135.6	0.940
0.2	96.2	1.5.E+06	0.926	113.7	4.9E+12	0.950	166.1	1.5E+16	0.820	145.1	0.978
0.3	113.7	4.9.E+06	0.900	131.1	1.6E+13	0.924	253.5	2.1E+22	0.830	170.2	0.990
0.4	148.6	4.1.E+08	0.940	166.1	3.6E+15	0.960	323.5	5.3E+27	0.720	210.3	0.949
0.5	157.4	1.9.E+09	0.960	174.9	6.3E+15	0.998	332.2	3.4E+27	0.610	212.5	0.960
0.6	155.6	1.8.E+08	0.997	174.9	1.6E+15	0.925	410.9	1.7E+27	0.820	226.3	0.990
0.7	131.1	6.7.E+06	0.907	153.9	2.2E+13	0.934	288.5	7.8E+22	0.900	197.3	0.990
0.8	157.4	1.0.E+08	0.900	174.9	3.4E+14	0.920	288.5	5.6E+09	0.850	231.3	0.992
0.9	122.4	3.7.E+03	0.800	157.4	7.2E+14	0.899	209.8	4.4E+09	0.990	191.9	0.999
Avg.	130.0	3.0.E+08	0.922	151.2	1.4E+15	0.943	261.3	1.1E+27	0.816	191.2	0.976
ZIF/WP20 sample											
0.1	104.9	1.2E+08	0.960	131.1	3.9E+14	0.970	69.9	8.9E+08	0.899	158.6	0.970
0.2	104.9	4.1E+06	0.920	122.4	1.3E+13	0.940	166.1	1.5E+16	0.889	160.2	0.990
0.3	157.4	1.5E+10	0.950	174.9	1.3E+17	0.963	323.5	4.3E+23	0.778	229.5	0.980
0.4	166.1	8.2E+09	0.860	174.9	2.7E+16	0.960	297.3	7.1E+26	0.886	246.9	0.990
0.5	236.1	2.3E+15	0.960	253.5	7.6E+21	0.965	463.4	6.8E+28	0.742	327.4	0.985
0.6	174.9	2.7E+10	0.970	201.1	8.8E+16	0.968	279.8	3.4E+28	0.784	253.4	0.990
0.7	174.9	2.7E+09	0.880	192.3	2.4E+16	0.868	384.7	1.6E+24	0.969	268.0	0.990
0.8	139.9	5.1E+06	0.860	166.1	1.7E+13	0.888	367.2	3.4E+14	0.995	260.8	0.890
0.9	174.9	1.1E+07	0.890	236.1	3.6E+13	0.923	306.0	2.6E+14	0.996	268.3	0.999
Avg.	159.3	2.6E+14	0.917	183.6	8.5E+20	0.938	295.3	1.1E+28	0.882	241.5	0.976
ZIF/WP30 sample											
0.1	78.7	1.1E+05	0.838	96.2	9.7E+11	0.893	69.9	3.3E+08	0.974	132.5	0.996
0.2	78.7	2.7E+04	0.806	96.2	9.0E+10	0.868	148.6	2.7E+14	0.980	137.0	0.988
0.3	87.4	3.3E+04	0.806	109.3	1.1E+11	0.888	244.8	2.9E+21	0.956	152.2	0.975
0.4	139.9	5.6E+07	0.847	157.4	1.8E+14	0.832	332.2	1.4E+28	0.959	220.0	0.990
0.5	104.9	8.8E+04	0.759	122.4	1.1E+11	0.757	306.0	2.3E+25	0.977	175.9	0.970
0.6	148.6	6.7E+07	0.800	166.1	2.2E+14	0.888	410.9	1.1E+25	0.990	243.0	0.980
0.7	96.2	6.1E+03	0.807	122.4	2.0E+10	0.785	183.6	4.4E+14	0.804	190.5	0.900
0.8	104.9	2.8E+03	0.985	131.1	5.6E+09	0.990	148.6	1.1E+11	0.996	153.1	0.924
0.9	244.8	8.9E+10	0.895	271.0	2.9E+17	0.889	419.7	1.4E+26	0.990	379.9	0.998
Avg.	120.5	9.9E+09	0.838	141.3	3.2E+16	0.866	251.6	1.6E+27	0.959	198.2	0.969

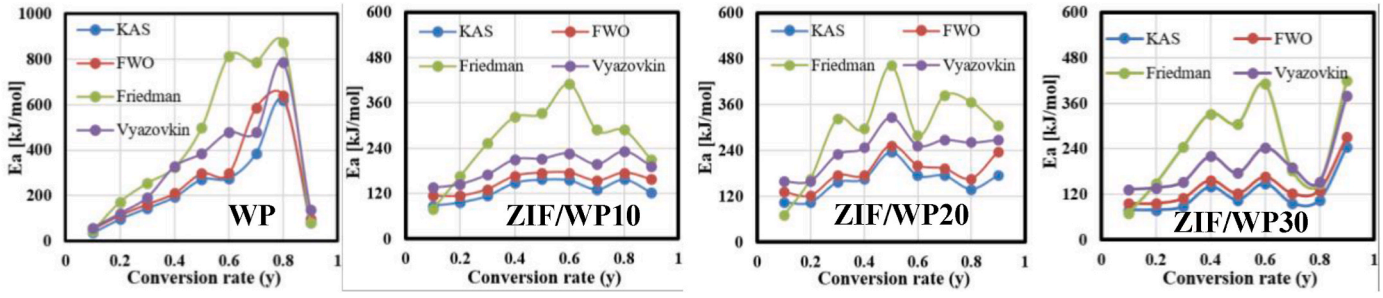

Figure (9). Pyrolytic activation energy of ZIF/WP samples at each conversion rate.

apparent activation energy with the conversion, resulting in greater variability in the FM-derived kinetic parameters. In contrast, the integral isoconversional methods (KAS and FWO) average the reaction behavior over a wider conversion range, producing smoother activation energy profiles [72,73]. Simultaneously, the A factor varied consistently with the kinetic compensation effect, where changes in Ea are accompanied by corresponding changes in A. This behavior reflects modifications in the apparent decomposition pathway rather than a direct measure of the connection of cobalt active sites. Moreover, the reaction order remained relativity unchanged among the investigated samples, suggesting that ZIF-67 primarily altered the energetic requirements of biomass decomposition without fundamentally changing that the global reaction mechanism. Since the kinetic parameters were derived from TGA analysis, they represent global apparent kinetics and should not be interpreted quantitative in terms of cobalt active-site density ore pore adsorption capacity without complementary catalyst characterization. On the other hand, the average Ea values of ZIF/WP samples calculated using VN model was estimated at 191.2 kJ/mol (ZIF/WP10),

241.5 kJ/mol (ZIF/WP20), and 198.2 kJ/mol (ZIF/WP30) exhibit R^2 ranging 0.969-0.976. The iterations needed to reach these optimal Ea values using VN model is summarized in Table 5, while the VN relationships of ZIF/WP samples are shown in Fig. (8). Compared to the average Ea of WP (233-427 kJ/mol), the ZIF/WP samples showed lower Ea values what means the present of ZIF-67 in the reaction not only upgrade the chemical products but also can decrease the complexity of reaction significantly. Among the isoconversional linear kinetic methods, the FWO model provided the most reliable description of the ZIF/WP samples with R^2 value of 0.938 for the optimum ZIF/WP20 sample. Furthermore, the nonlinear Vyazovkin method exhibited the highest fitting accuracy ($R^2 = 0.976$) and therefore considered the most suitable kinetic approach for describing the thermal decomposition behavior for the ZIF/WP samples.

3.6. Thermodynamic analysis

The thermodynamic parameters were evaluated for the ZIF/WP20 sample (at 20 °C/min) because this catalyst loading produced the higher relative $C_{16}H_{16}$ content among the investigated samples, as identified by the GC-MS analysis. The results were subsequently compared with those of the non-catalytic WP sample to assess the influence of ZIF-67 on the thermodynamic characteristic of the pyrolysis process. The thermodynamic parameters (ΔH, ΔG, and ΔS) of the WP and ZIF/WP20 samples were calculated using **Eqs.** [7–9], and the obtained values are presented in Table 6. For the WP sample, ΔH ranged from 228 to 422 kJ/mol, ΔG from 165 to 316 kJ/mol, and ΔS from 0.036 to 0.165 kJ/mol K. In comparison, the ZIF/WP20 sample exhibited lower values, with ΔH ranging from 154 to 290 kJ/mol, ΔG from 149 to 206 kJ/mol, and ΔS from −0.081 to 0.136 kJ/mol K. The positive ΔH values obtained from both samples confirm that the pyrolysis process is endothermic and needs continuous heat input to proceed. However, the significantly lower ΔH values of the ZIF/WP20 sample indicate that the presence of ZIF-67 reduces the energy required for thermal decomposition, thereby enhancing the reaction efficiency. Likewise, the positive ΔG values demonstrate that the decomposition reactions are non-spontaneous and needs external energy input to overcome the Ea barrier, which is characteristic of biomass pyrolysis process [74]. The ΔS exhibited both negative and positive values depending on the conversion rate. Negative ΔG values indicate that the activated complex processes a higher degree of order than the reactants, suggesting stronger interactions between biomass derived intermediates and the catalytic active sites of ZIF-67, which reduce molecular freedom during the early stages of decomposition. As the conversion progresses, ΔS becomes positive, indicating the formation of a less order transition state due to extensive bond cleavage, generation of volatile intermediates [75], and increased molecular mobility associated with secondary cracking and aromatization reactions. These results suggest that the catalytic pyrolysis proceeds through multiple reaction pathways with different transition state characteristics over the conversion range.

3.7. Artificial neural networks analysis

The optimized ANN model was used to predict the thermal decomposition of WP and ZIF/WP samples at unmeasured TGA conditions, at 18 °C/min. The ANN features of WP and ZIF/WP20 sample (that provided the optimal mixing sample) is shown in Figs. 10 and 11, the while the ANN features of ZIF/WP10 and ZIF/WP30 samples were moved to Supplementary materials (Figs. (S3, S4)). The ANN properties show a significant decrease in MSE value with the best validation behaviour of 0.036998 at epoch 14 (WP) and 0.01068 at epoch 61 (ZIF/WP20) (Figs. (10A, 11A)). The ANN simulation process exhibited predictive accuracy, as evidenced by the high correlation coefficients obtained during the training and validation stage. The R^2 were in the ranges of 0.99994-0.99998 (WP) and 0.99999 (ZIF/WP20) for the training, validation, test, and all datasets (Figs. (10B-E,11B-E)). These findings demonstrate that the optimal model effectively captures the main decomposition traits of WP and ZIF/WP samples. The error distribution histogram in Figs. (10F,11F), based on 20 bins is roughly normal, with residuals ranging from −0.1719 to 0.1388 (WP) and −0.01728 to 0.03311 (ZIF/WP20). The WP and ZIF/WP samples distribution stays close to the zero-error line and well within the ±1 acceptable error range reported for such cases [76]. This conforms the ANN model's high accuracy and reliability in predicting WP and ZIF/WP decomposition. Fig. (10G, 11G) represents the full training dataset alongside the model's predictions. To further assets the predictive capability of the constructed model, the optimized ANN algorithm was employed to simulate the thermal degradation behaviour of WP and ZIF/WP20 sample at a heating rate of 18 °C/min. The predicated results were then compared with the corresponding experimental TGA data, as presented in Fig. (12). A remarkable agreement between the predicted and experimental decomposition patterns was observed, with the model predictions consistently falling within the experimental confidence boundaries. This excellent correspondence validates the reliability of the ANN model, confirming its effectiveness in accuracy describing and predicting the thermal degradation properties of WP and ZIF/WP samples under unknow operating conditions. It should be noted that the developed ANN models were trained exclusively using TGA data. Consequently, the models are capable of predicting the thermal decomposition behaviour of the WP and ZIF/WP samples but cannot predict the yield or composition of individual pyrolysis products, including C16H16. The development of an ANN model capable of predicting and distribution of specific pyrolysis products would require a comprehensive experimental database containing the quantitative yields of individual compounds under various operating conditions, including pyrolysis temperature, heating rate, catalyst loading, and vapor residence time. Such an investigation is beyond the scope of the present study but represents an important direction for future research.

Table 5
Activation energies of ZIF/WP samples calculated via VN model.

y	First Iteration (kJ/mol)	Second Iteration (kJ/mol)	Third iteration (kJ/mol)	Fourth iteration (kJ/mol)	First Iteration (kJ/mol)	Second Iteration (kJ/mol)	Third iteration (kJ/mol)	Fourth iteration (kJ/mol)	First Iteration (kJ/mol)	Second Iteration (kJ/mol)	Third iteration (kJ/mol)	Fourth iteration (kJ/mol)
	10 wt% ZIF-67 sample				20 wt% ZIF-67 sample				30 wt% ZIF-67 sample			
0.1	139.5	147.8	135.6	135.6	158.4	160.3	158.6	158.6	134.0	135.0	134.0	134.0
0.2	144.7	145.1	145.1	145.1	160.2	160.2	160.2	160.2	138.7	138.6	138.6	138.6
0.3	170.3	170.2	170.2	170.2	228.7	229.5	229.5	229.5	154.0	153.9	153.9	153.9
0.4	210.2	210.3	210.3	210.3	246.8	246.8	246.9	246.9	222.4	222.4	222.4	222.4
0.5	212.5	212.5	212.5	212.5	327.4	320.8	327.4	327.4	177.9	177.8	177.8	177.8
0.6	226.3	226.3	226.3	226.3	253.4	253.4	253.4	253.4	245.7	245.7	245.7	245.7
0.7	197.4	197.4	197.3	197.3	267.4	268.0	268.0	268.0	192.7	192.7	192.7	192.7
0.8	231.3	231.3	231.3	231.3	260.0	260.7	260.8	260.8	154.8	154.8	154.8	154.8
0.9	191.9	191.9	191.9	191.9	268.2	268.3	268.3	268.3	383.9	384.1	384.1	384.1
Average	191.6	192.5	191.2	191.2	241.2	240.9	241.5	241.5	200.4	200.5	200.4	200.4

Table 6
Thermodynamic parameters of WP and ZIF/WP20 samples.

y	KAS			FWO			FM		
	ΔH (kJ/mol)	ΔG (kJ/mol)	ΔS kJ/(mol K)	ΔH (kJ/mol)	ΔG (kJ/mol)	ΔS kJ/(mol K)	ΔH (kJ/mol)	ΔG (kJ/mol)	ΔS kJ/(mol K)
WP sample									
0.1	30	166	−0.213	47	114	−0.105	38	132	−0.146
0.2	91	184	−0.146	108	124	−0.025	166	166	0.000
0.3	139	191	−0.082	156	129	0.043	248	135	0.176
0.4	187	200	−0.020	204	132	0.113	318	144	0.271
0.5	266	201	0.101	292	147	0.226	493	151	0.534
0.6	270	207	0.098	291	154	0.214	808	175	0.988
0.7	379	222	0.245	580	338	0.378	782	854	−0.112
0.8	615	247	0.576	633	184	0.700	869	884	−0.023
0.9	73	223	−0.233	91	160	−0.108	73	201	−0.199
Avg.	228	205	0.036	267	165	0.160	422	316	0.165
ZIF/WP20 sample									
0.1	100	167	−0.105	126	113	0.020	65	121	−0.088
0.2	100	185	−0.133	117	123	−0.009	161	129	0.050
0.3	152	194	−0.065	170	126	0.068	318	194	0.193
0.4	161	206	−0.070	170	134	0.055	292	128	0.254
0.5	231	209	0.034	248	146	0.159	458	270	0.292
0.6	170	208	−0.060	196	154	0.065	274	90	0.287
0.7	170	220	−0.079	187	152	0.054	379	248	0.204
0.8	135	219	−0.131	161	165	−0.006	362	350	0.019
0.9	170	250	−0.125	231	231	0.000	301	290	0.016
Avg.	154	206	−0.081	178	149	0.045	290	202	0.136

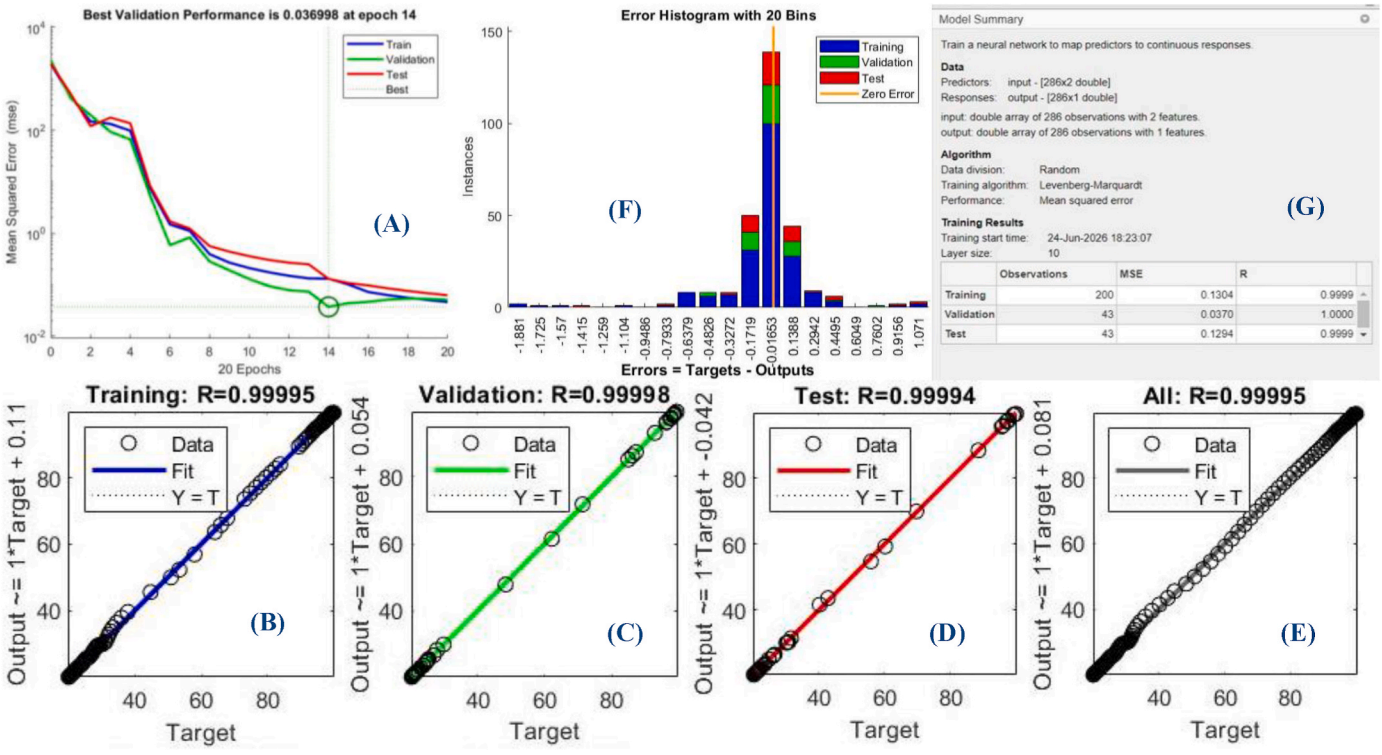

Figure (10). Artificial neural network characterises of WP sample.

4. Conclusions

In this research, the pyrolysis behaviour of wood pellets (WP) biomass over different loading of ZIF-67 as a promising flexible catalyst (ZIF/WP) was study using TGA, TG-FTIR, and GC/MS analytical systems. The kinetic and thermodynamic properties of ZIF/WP samples was modelled, allowing to determine the potential effect of using ZIF-67 on reduction the complexity of WP decomposition. Also, the thermal degradation of ZIF/WP samples under unknown operating pyrolysis conditions were simulated by developed artificial neural network (ANN) model. The TGA results showed that including ZIF-67 catalyst to the reaction did not change the WP decomposition features that decomposed completely at 600 °C with overall total weight loss ranging 77-86 wt%. The same features were noticed in TG-FTIR, where C=O stretching of carbonyl groups and CO_2 asymmetric stretching vibration were main functional groups of the released vapors even with changing catalyst concentration. Whereas the significant changes were observed in GC/MS that showed that the vapors are rich in naphthalene, 1,2,3,4 tetrahydro-2-phenyl- ($C_{16}H_{16}$), especially in case ZIF/WP20 with abundance reached up to 85% at 20 °C/min. These results confirm that

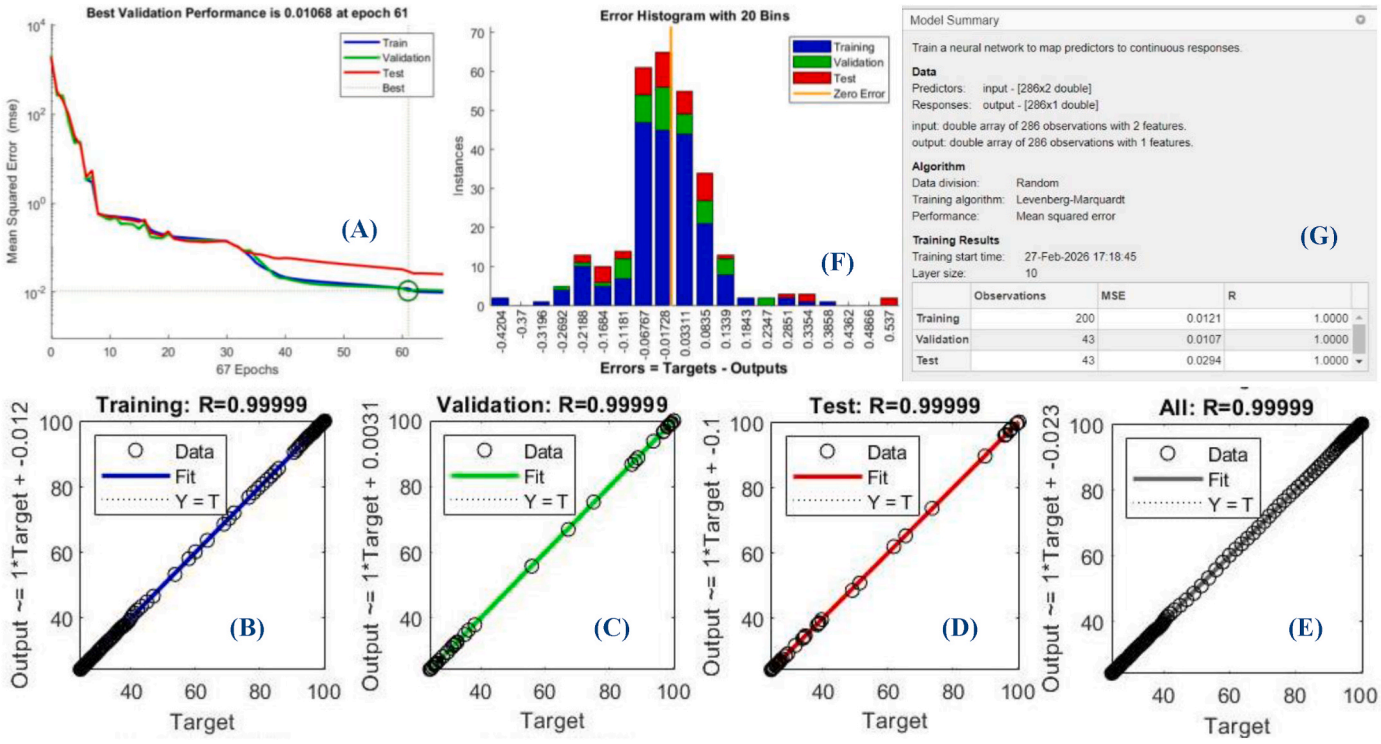

Figure (11). Artificial neural network characterises of ZIF/WP20 sample.

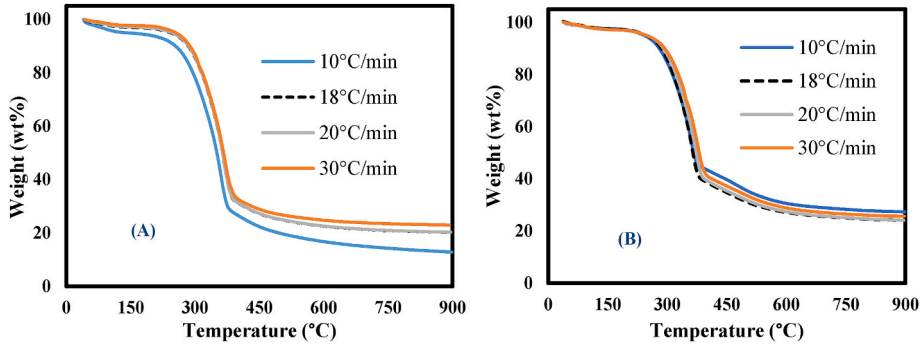

Figure (12). TGA patterns of A) PW and B) ZIF/WP20 samples based on prediction the optimized ANN model.

ZIF-67 can help significantly in converting the complex chemical compounds of biomass pyrolytic vapors (like aldehydes, ketones, alcohols, furans, and phenolic derivatives, etc.) into high added value products. In addition, its significant contribution to reduce the activation energy from 233 to 427 kJ/mol (WP) to 130-261.3 kJ/mol (ZIF/WP10), 159.3-295.3 kJ/mol (ZIF/WP20), and 120.5-251.6 kJ/mol (ZIF/WP30). Finally, the developed ANN model exhibited high potential validation, reliability, and describing ZIF/WP degradation with predicting efficiency reached up to 0.99999. These results demonstrate that ZIF-67 has a high future potential in upgrading the biomass pyrolysis products and reduce its reaction decomposition and convert it into $C_{16}H_{16}$ that has a wieldy used in several industrial applications, which supporting its future biomass upgrading.

CRediT authorship contribution statement

Samy Yousef: Conceptualization, Data curation, Formal analysis, Funding acquisition, Investigation, Methodology, Project administration, Resources, Software, Supervision, Validation, Visualization, Writing – original draft, Writing – review & editing. **Vilmantė Kudelytė:** Conceptualization, Data curation, Formal analysis, Investigation. **Nerijus Striūgas:** Conceptualization, Data curation, Formal analysis, Resources. **Mohammed Ali Abdelnaby:** Conceptualization, Data curation, Formal analysis, Investigation, Software.

Declaration of competing interest

The authors declare that they have no known competing financial interests or personal relationships that could have appeared to influence the work reported in this paper.

Acknowledgment

This publication is based upon work from COST Action CA22147, European metal-organic framework network: combining research and development to promote technological solutions (EU4MOFs)“, supported by COST (European Cooperation in Science and Technology).

Appendix A. Supplementary data

Supplementary data to this article can be found online at https://doi.org/10.1016/j.biombioe.2026.109868.

Data availability

The data that has been used is confidential.

References

[1] https://joint-research-centre.ec.europa.eu/jrc-news-and-updates/rise-biomass-production-and-use-points-growing-bioeconomy-resource-limitless-2023-12-11_en.
[2] M. Antar, D. Lyu, M. Nazari, A. Shah, X. Zhou, D.L. Smith, Biomass for a sustainable bioeconomy: an overview of world biomass production and utilization, Renew. Sustain. Energy Rev. 139 (2021) 110691, https://doi.org/10.1016/j.rser.2020.110691.
[3] N. Srivastava, A. Shrivastav, R. Singh, M. Abohashrh, K.R. Srivastava, S. Irfan, M. Srivastava, P.K. Mishra, V.K. Gupta, V.K. Thakur, Advances in the structural composition of biomass: fundamental and bioenergy applications, J. Renew. Mater. 9 (4) (2021) 615–636, https://doi.org/10.32604/jrm.2021.014374.
[4] M. Namakka, M.R. Rahman, M.K.B. Bakri, Waste biomass pellets for green energy production - a sustainable alternative for energy security, Renew. Sustain. Energy Rev. 226 (2025) 116315, https://doi.org/10.1016/j.rser.2025.116315.
[5] O. Svedovs, A. Sturmane, M. Feofilovs, V. Kirsanovs, F. Romagnoli, Comparative cradle-to-grave life cycle assessment of wood and alternative biomass pellet feedstocks for decentralized heating using experimental data, Biomass Bioenergy 208 (2025) 108880, https://doi.org/10.1016/j.biombioe.2025.108880.
[6] A. Tshikovhi, T.E. Motaung, Technologies and innovations for biomass energy production, Sustainability 15 (16) (2023) 12121, https://doi.org/10.3390/su151612121.
[7] C.K. Khanal, S. Kafle, S. Adhikari, A critical review of techno-economic analysis for producing transportation fuel from biomass pyrolysis, Biomass Bioenergy 209 (2026) 108985, https://doi.org/10.1016/j.biombioe.2026.108985.
[8] W. Ahmad, J. Nisar, F. Anwar, F. Muhammad, Future prospects of biomass waste as renewable source of energy in Pakistan: a mini review, Bioresour. Technol. Rep. 24 (2023) 101658, https://doi.org/10.1016/j.biteb.2023.101658.
[9] C. Ma, J. Hu, H. Wang, Y. Yu, C. Tan, Advances and challenges in biomass thermochemical conversion: from resource utilization to process optimization, Renew. Sustain. Energy Rev. 226 (2025) 116385, https://doi.org/10.1016/j.rser.2025.116385.
[10] D. Lachos-Perez, J.C. Martins-Vieira, J. Missau, K. Anshu, O.K. Siakpebru, S. K. Thengane, A.R.C. Morais, E.H. Tanabe, D.A. Bertuol, Review on biomass pyrolysis with a focus on bio-oil upgrading techniques, Analytica—A Journal of Analytical Chemistry and Chemical Analysis 4 (2) (2023) 182–205, https://doi.org/10.3390/analytica4020015.
[11] X. Hu, M. Gholizadeh, Biomass pyrolysis: a review of the process development and challenges from initial researches up to the commercialisation stage, J. Energy Chem. 39 (2019) 109–143, https://doi.org/10.1016/j.jechem.2019.01.024.
[12] D. Zilberman, D. Laird, C. Rainey, J. Song, G. Kahn, Biocharsupply-chainand challenges to commercialization, GCB Bioenergy 15 (1) (2022) 7–23, https://doi.org/10.1111/gcbb.12952.
[13] H.E. Ouahabi, O. Bayessi, A. Mouaky, A. Hirt, S. Rachidi, Biochar revolution: harnessing pyrolysis for climate resilience and circular environmental solutions, Carbon Trends 23 (2026) 100628, https://doi.org/10.1016/j.cartre.2026.100628.
[14] A.N. Amenaghawon, C.L. Anyalewechi, C.O. Okieimen, H.S. Kusuma, Biomass pyrolysis technologies for value-added products: a state-of-the-art review, Environ. Dev. Sustain. 23 (10) (2021) 14324–14378, https://doi.org/10.1007/s10668-021-01276-5.
[15] H.E. Farissi, A. Choukoud, A.E. Kasmi, B. Manoun, F. Cacciola, T. Chafik, M. G. Perez, Innovative transition from traditional pyrolysis to catalytic pyrolysis for bioenergy: optimizing bio-oil production from renewable biomass, Biomass Bioenergy 208 (2025) 108850, https://doi.org/10.1016/j.biombioe.2025.108850.
[16] P. Yan, H. Peng, H. Rabiee, L. Ge, Y. Weng, B. Ma, J. Wang, M. Konarova, G. Zhao, E.M. Kennedy, Z. Zhu, M. Stockenhuber, Advances in lignocellulosic biomass pyrolysis and catalytic upgrading for sustainable biofuel production: process design strategies and reaction rationales, Green Chem. 27 (35) (2025) 10444–10477, https://doi.org/10.1039/d5gc02199e.
[17] T.K. Dada, M. Sheehan, S. Murugavelh, et al., A review on catalytic pyrolysis for high-quality bio-oil production from biomass, Biomass Convers. Biorefinery 13 (2023) 2595–2614, https://doi.org/10.1007/s13399-021-01391-3.
[18] C.J. Wrasman, A.N. Wilson, O.D. Mante, K. Iisa, A. Dutta, M.S. Talmadge, D. C. Dayton, S. Uppili, M.J. Watson, X. Xu, M.B. Griffin, C. Mukarakate, J. A. Schaidle, M.R. Nimlos, Catalytic pyrolysis as a platform technology for supporting the circular carbon economy, Nat. Catal. 6 (7) (2023) 563–573, https://doi.org/10.1038/s41929-023-00985-6.
[19] W. Sun, Y. Yan, Y. Wei, J. Ma, Z. Niu, G. Hu, Catalytic pyrolysis of biomass: a review of zeolite, carbonaceous, and metal oxide catalysts, Nanomaterials 15 (7) (2025) 493, https://doi.org/10.3390/nano15070493.
[20] R.K. Mishra, S.M. Chistie, S.U. Naika, K. Mohanty, Catalytic pyrolysis of biomass over zeolites for bio-oil and chemical production: a review on their structure, porosity and acidity co-relation, Bioresour. Technol. 366 (2022) 128189, https://doi.org/10.1016/j.biortech.2022.128189.
[21] B. Zhang, Z. Wang, L. Gao, X. Zhong, Y. Zhang, M. Shakeri, X. Zhang, Accurately tuning the pore size and acidity of mesoporous zeolites for enhancing the catalytic hydrocracking of polypropylene, J. Mater. Chem. A 13 (4) (2024) 2875–2883, https://doi.org/10.1039/d4ta07329k.
[22] I.M.S. Anekwe, Y.M. Isa, Unlocking catalytic longevity: a critical review of catalyst deactivation pathways and regeneration technologies, Energy Adv. 4 (9) (2025) 1075–1113, https://doi.org/10.1039/d5ya00015g.
[23] M.S. Alhumaimess, Metal–organic frameworks and their catalytic applications, J. Saudi Chem. Soc. 24 (6) (2020) 461–473, https://doi.org/10.1016/j.jscs.2020.04.002.
[24] A. Rapeyko, F.X. Llabrés i Xamena, Zirconium-containing metal–organic frameworks (MOFs) as catalysts for biomass conversion, Appl. Sci. 15 (5) (2025) 2609, https://doi.org/10.3390/app15052609.
[25] C. Pownraj, A. Karthik, B. Prabhu, S. Suresh, K. Yatish, J.K. Katiyar, A.V. Arasu, Effect of Cu MOF based functional catalysts on cracking and adsorption of bio-oil compounds via thermo-catalytic pyrolysis: a net zero emission scenario, Fuel 383 (2025) 133871, https://doi.org/10.1016/j.fuel.2024.133871.
[26] N.J. Rubinsin, W.N.R.W. Isahak, S. Samidin, M. Pudukudy, M.A. Nemitallah, N. A. Karim, Gas product behaviour using flower-like nickel-based MOF catalysts for sustainable hydrogen production from biomass, Renew. Energy (2025) 122886, https://doi.org/10.1016/j.renene.2025.122886.
[27] X. Song, S. Liu, T. Li, H. Wang, F. Huang, X. Bai, D. Bi, Enriching pyrrole components in bio-oil by nitrogen-rich pyrolysis of tobacco stem employing ZIF-67/ZSM-5 dual-catalyst, J. Anal. Appl. Pyrolysis (2025) 107212, https://doi.org/10.1016/j.jaap.2025.107212.
[28] X. Zhou, Z. Zhang, Metal organic frameworks catalytic co-pyrolysis mechanism of waste wood and rubber for oil preparation, J. Energy Inst. (2025) 102285, https://doi.org/10.1016/j.joei.2025.102285.
[29] S. Wan, C. Chen, R. Yang, S. Zhao, S. He, X. Zhao, Co-pyrolysis characteristics and pyrolysis oil analysis of Chlorella vulgaris and marine waste plastics with multi-metal MOFs-derived additive, Chem. Eng. J. 498 (2024) 154854, https://doi.org/10.1016/j.cej.2024.154854.
[30] H. Wu, W. Deng, M. Hu, Y. Su, Catalytic decomposition of pyrolysis vapors from microwave pyrolysis of sewage sludge over MOF-derived catalysts toward low-nitrogen bio-oil, Energy Convers. Manag. 346 (2025) 120435, https://doi.org/10.1016/j.enconman.2025.120435.
[31] X. Duan, S. Yan, Y. Li, S. Fang, X. Tie, H. Wang, H. Wang, J. Liu, C. Zou, T. Wang, W. Feng, Preparation of chromium-doped ZIFs-8/ZnCo-LDH composite as a acid-base bifunctional catalyst for biodiesel production, Renew. Energy 238 (2024) 121940, https://doi.org/10.1016/j.renene.2024.121940.
[32] Y. Chen, X. Wu, H. Chen, W. Chen, J. Hu, C. Chang, S. Pang, P. Li, Production of MAH-rich bio-oil from co-pyrolysis of biomass and plastics using carbonized MOF catalysts under microwave irradiation, Energy 313 (2024) 134049, https://doi.org/10.1016/j.energy.2024.134049.
[33] J. Hashemibeni, J. Eimontas, N. Striūgas, G. Janušas, A. Bronušienė, M. A. Abdelnaby, Pyrolysis characteristics of metal-organic frameworks: TG-FTIR, TG-GC-MS, kinetic, thermodynamic and artificial neural network modelling, J. Anal. Appl. Pyrolysis 193 (2025) 107431, https://doi.org/10.1016/j.jaap.2025.107431.
[34] S. Yousef, J. Eimontas, N. Striūgas, V. Kudelytė, M.A. Abdelnaby, Thermal stability and decomposition pathways of zeolitic imidazolate frameworks for future catalytic thermochemical applications, J. Anal. Appl. Pyrolysis 197 (2026) 107839, https://doi.org/10.1016/j.jaap.2026.107839.
[35] Y. Huang, Y. Chen, M. Xu, A. Ly, A. Gili, E. Murphy, T. Asset, Y. Liu, V. De Andrade, C.U. Segre, A.L. Deriy, F. De Carlo, M. Kunz, A. Gurlo, X. Pan, P. Atanassov, I. V. Zenyuk, Catalysts by pyrolysis: transforming metal-organic frameworks (MOFs) precursors into metal-nitrogen-carbon (M-N-C) materials, Mater. Today 69 (2023) 66–78, https://doi.org/10.1016/j.mattod.2023.08.007.
[36] S. Kouser, A. Hezam, M.J.N. Khadri, et al., A review on zeolite imidazole frameworks: synthesis, properties, and applications, J. Porous Mater. 29 (2022) 663–681, https://doi.org/10.1007/s10934-021-01184-z.
[37] S. Dutta, M. Walden, A. Sinelshchikova, R. Ettlinger, E. Lizundia, S. Wuttke, Cradle-to-Gate environmental impact assessment of commercially available metal-organic frameworks manufacturing, Adv. Funct. Mater. 34 (52) (2024), https://doi.org/10.1002/adfm.202410751.
[38] S. Yousef, Techno-economic assessment of scale-up of metal-organic framework production, J. Indian Chem. Soc. 102 (12) (2025) 102316, https://doi.org/10.1016/j.jics.2025.102316.
[39] O. Bongomin, C. Nzila, J.I. Mwasiagi, O. Maube, Comprehensive thermal properties, kinetic, and thermodynamic analyses of biomass wastes pyrolysis via TGA and Coats-Redfern methodologies, Energy Convers. Manag. X 24 (2024) 100723, https://doi.org/10.1016/j.ecmx.2024.100723.
[40] N. Agnihotri, M.K. Mondal, Thermal analysis, kinetic behavior, reaction modeling, and comprehensive pyrolysis index of soybean stalk pyrolysis, Biomass Convers. Biorefinery 14 (2024) 14977–14992, https://doi.org/10.1007/s13399-023-03807-8.
[41] C.N. Arenas, M.V. Navarro, J.D. Martínez, Pyrolysis kinetics of biomass wastes using isoconversional methods and the distributed activation energy model, Bioresour. Technol. 288 (2019) 121485, https://doi.org/10.1016/j.biortech.2019.121485.
[42] N. Striūgas, J. Eimontas, M.A. Abdelnaby, Synthesis of benzoic acid from catalytic co-pyrolysis of waste wind turbine blades and biomass and their kinetic analysis, J. Anal. Appl. Pyrolysis 182 (2024) 106684, https://doi.org/10.1016/j.jaap.2024.106684.
[43] S. Wang, K. Wu, J. Yu, B. Luo, C. Chu, H. Zhang, Kinetic and thermodynamic analysis of biomass catalytic pyrolysis with nascent biochar in a two-stage reactor,

Combust. Flame 251 (2023) 112671, https://doi.org/10.1016/j.combustflame.2023.112671.
[44] N.J. Striūgas, K. Meile, M.A. Abdelnaby, Co-pyrolysis of Baltic wheat straw and low-density polyethylene bags and its kinetic and thermodynamic behaviour, Ind. Crop. Prod. 218 (2024) 118970, https://doi.org/10.1016/j.indcrop.2024.118970.
[45] K. Laouidi, S. Habchi, C.K. Fanezoune, B. Sallek, N. Kussul, H.E. Bari, Advancements in artificial neural networks and fast pyrolysis of biomass processing: a comprehensive review and a bibliometric analysis, J. Anal. Appl. Pyrolysis 189 (2025) 107098, https://doi.org/10.1016/j.jaap.2025.107098.
[46] S. Yousef, J. Eimontas, N. Striūgas, M.A. Abdelnaby, Co-pyrolysis of waste wind turbine blades and biomass and their kinetic analysis using artificial neural network, J. Anal. Appl. Pyrolysis 179 (2024) 106495, https://doi.org/10.1016/j.jaap.2024.106495.
[47] Y. Wang, S. Yang, G. Bao, H. Wang, Pyrolytic characteristics of abutilon stalk waste using TG-FTIR, Py-GC/MS, and artificial neural networks: kinetics, thermodynamics, and gaseous products distribution, J. Anal. Appl. Pyrolysis 178 (2024) 106403, https://doi.org/10.1016/j.jaap.2024.106403.
[48] V. Kudelytė, J. Eimontas, N. Striūgas, M.A. Abdelnaby, Pyrolysis and ANN-based modeling of copper-impregnated nylon fishing net waste, Sustain. Chem. Pharm. 46 (2025) 102054, https://doi.org/10.1016/j.scp.2025.102054.
[49] A. Sahoo, R. Gautam, S. Kumar, K. Mohanty, Energy optimization from a binary mixture of non-edible oilseeds pyrolysis: kinetic triplets analysis using Thermogravimetric Analyser and prediction modeling by Artificial Neural Network, J. Environ. Manag. 297 (2021) 113253, https://doi.org/10.1016/j.jenvman.2021.113253.
[50] G. Gerandi, A. Brillard, V. Tschamber, Multi-scale thermal degradation of wood pellets under low heating rates: experiments and modeling, Bioresour. Technol. 407 (2024) 131132, https://doi.org/10.1016/j.biortech.2024.131132.
[51] M. Poletto, A.J. Zattera, R.M. Santana, Thermal decomposition of wood: kinetics and degradation mechanisms, Bioresour. Technol. 126 (2012) 7–12, https://doi.org/10.1016/j.biortech.2012.08.133.
[52] R. Barzegar, A. Yozgatligil, H. Olgun, A.T. Atimtay, TGA and kinetic study of different torrefaction conditions of wood biomass under air and oxy-fuel combustion atmospheres, J. Energy Inst. 93 (3) (2019) 889–898, https://doi.org/10.1016/j.joei.2019.08.001.
[53] M.M. Jaffar, M.A. Nahil, P.T. Williams, Pyrolysis-catalytic hydrogenation of cellulose-hemicellulose-lignin and biomass agricultural wastes for synthetic natural gas production, J. Anal. Appl. Pyrolysis 145 (2019) 104753, https://doi.org/10.1016/j.jaap.2019.104753.
[54] J. Eimontas, N. Striūgas, M.A. Abdelnaby, Pyrolysis and gasification kinetic behavior of mango seed shells using TG-FTIR-GC–MS system under N2 and CO2 atmospheres, Renew. Energy 173 (2021) 733–749, https://doi.org/10.1016/j.renene.2021.04.034.
[55] A. Vilas-Boas, L. Tarelho, J. Moura, H. Gomes, C. Marques, D. Pio, M. Nunes, A. Silvestre, Methodologies for bio-oil characterization from biomass pyrolysis: a review focused on GC-MS, J. Anal. Appl. Pyrolysis 185 (2024) 106850, https://doi.org/10.1016/j.jaap.2024.106850.
[56] X. Liu, Z. Liu, R. Wang, Functionalized metal-organic framework catalysts for sustainable biomass valorization, Adv. Polym. Technol. (2020) 1–11, https://doi.org/10.1155/2020/1201923, 2020.
[57] C. Romero-Unda, K.J. Fernández-Andrade, F. Vallejo, S. Alejandro-Martín, Enhanced aromatic hydrocarbon production from biomass-plastic co-hydropyrolysis over Ni/MOF-derived catalyst, Ind. Crop. Prod. 226 (2025) 120749, https://doi.org/10.1016/j.indcrop.2025.120749.
[58] A. Hart, M. Adam, J.P. Robinson, S.P. Rigby, J. Wood, Hydrogenation and dehydrogenation of tetralin and naphthalene to explore heavy oil upgrading using NiMo/Al2O3 and CoMo/Al2O3 catalysts heated with steel balls via induction, Catalysts 10 (5) (2020) 497, https://doi.org/10.3390/catal10050497.
[59] H. Chang, J. Li, S. Du, K. Shen, Q. Yang, H. Yi, J. Zhang, Transformation characteristics of hydrogen-donor solvent tetralin in the process of direct coal liquefaction, Front. Chem. 7 (2019) 737, https://doi.org/10.3389/fchem.2019.00737.
[60] https://pubchem.ncbi.nlm.nih.gov/compound/1-Phenyl-1_2_3_4-tetrahydronaphthalene.
[61] J. Gancedo, L. Faba, S. Ordoñez, New approaches for obtaining renewable naphthalenes by acid-catalyzed diels-alder additions: the role of furan-aromatic condensations, Appl. Catal. A Gen. 685 (2024) 119907, https://doi.org/10.1016/j.apcata.2024.119907.
[62] D. Han, L. Sun, L. Chen, S. Yang, T. Li, X. Xie, M. Xu, W. Tang, B. Zhao, H. Si, D. Hua, Review on the progress in the production of aromatic hydrocarbons by co-catalytic pyrolysis of biomass and plastics, J. Fuel Chem. Technol. 52 (4) (2024) 481–495, https://doi.org/10.1016/s1872-5813(23)60401-3.
[63] M. Grojzdek, B. Novosel, D. Klinar, J. Golob, A.Ž. Gotvajn, Pyrolysis of different wood species: influence of process conditions on biochar properties and gas-phase composition, Biomass Convers. Biorefinery 14 (5) (2021) 6027–6037, https://doi.org/10.1007/s13399-021-01480-3.
[64] E. Ranucci, J. Alongi, Thermal decomposition of cellulosic materials: insights into mechanisms and product evolution, Polym. Degrad. Stabil. 242 (2025) 111629, https://doi.org/10.1016/j.polymdegradstab.2025.111629.
[65] A.Q. Nguyen, L.T.P. Trinh, Thermochemical conversion of cellulose and hemicellulose, in: N.P. Nghiem, T.H. Kim, C.G. Yoo (Eds.), Biomass Utilization: Conversion Strategies, Springer, Cham, 2022, https://doi.org/10.1007/978-3-031-05835-6_6.
[66] X. Lu, X. Gu, A review on lignin pyrolysis: pyrolytic behavior, mechanism, and relevant upgrading for improving process efficiency, Biotechnol. Biofuels 15 (2022) 106, https://doi.org/10.1186/s13068-022-02203-0.
[67] M. Yu, Y. Gao, R. Wang, W. Wu, J. Qiu, Y. Huang, J. Beiyuan, H. Cheng, Y. Zhao, Z. Cheng, H. Wang, Effects of lignin, hemicellulose, and cellulose of feedstock and pyrolytic temperature on the composition and properties of biochar-derived dissolved organic matter, J. Anal. Appl. Pyrolysis 194 (2025) 107572, https://doi.org/10.1016/j.jaap.2025.107572.
[68] Y. Cai, X. Liu, W. Yang, H. Peng, L. Meng, S. Zhao, Preparation of cobalt based metal organic framework ZIF-67 catalyst for activating peroxymonosulfate and its catalytic system for rapid degradation of Rhodamine B and other dyes at high concentrations, RSC Adv. 15 (58) (2025) 49875–49888, https://doi.org/10.1039/d5ra08184j.
[69] W. Xiong, S. Zhou, L. Wang, Y. Liu, F. Hao, P. Liu, H. Luo, ZIF-derived Co-Based catalysts for efficient hydrogenation of aromatic compounds: the study of the Co–Nx active sites, Ind. Eng. Chem. Res. 59 (52) (2020) 22473–22484, https://doi.org/10.1021/acs.iecr.0c04966.
[70] M. Praspaliauskas, J. Eimontas, N. Striūgas, M.A. Abdelnaby, Pyrolysis kinetic behaviour of glass fibre-reinforced epoxy resin composites using linear and nonlinear isoconversional methods, Polymers 13 (10) (2021) 1543, https://doi.org/10.3390/polym13101543.
[71] S. Yousef, J. Eimontas, N. Striūgas, M.A. Abdelnaby, Pyrolysis kinetic behaviour and TG-FTIR-GC–MS analysis of coronavirus face masks, J. Anal. Appl. Pyrolysis 156 (2021) 105118, https://doi.org/10.1016/j.jaap.2021.105118.
[72] S. Vyazovkin, Modern isoconversional kinetics: from misconceptions to advances, in: Handbook of Thermal Analysis and Calorimetry, 2018, pp. 131–172, https://doi.org/10.1016/b978-0-444-64062-8.00008-5.
[73] D. Trache, A. Abdelaziz, B. Siouani, A simple and linear isoconversional method to determine the pre-exponential factors and the mathematical reaction mechanism functions, J. Therm. Anal. Calorim. 128 (1) (2016) 335–348, https://doi.org/10.1007/s10973-016-5962-0.
[74] Z. Zhang, Y. Li, L. Luo, D. Yellezuome, M.M. Rahman, J. Zou, H. Hu, J. Cai, Insight into kinetic and thermodynamic analysis methods for lignocellulosic biomass pyrolysis, Renew. Energy 202 (2022) 154–171, https://doi.org/10.1016/j.renene.2022.11.072.
[75] A.K. Vuppaladadiyam, S.S.V. Vuppaladadiyam, S.S.V. Vuppaladadiyam, V. S. Sikarwar, E. Ahmad, K.K. Pant, M. S, A. Pandey, S. Bhattacharya, A. Sarmah, S. Leu, A critical review on biomass pyrolysis: reaction mechanisms, process modeling and potential challenges, J. Energy Inst. 108 (2023) 101236, https://doi.org/10.1016/j.joei.2023.101236.
[76] A. Fernandez, D. Zalazar-García, C. Lorenzo-Doncel, D.M.Y. Maya, E.E.S. Lora, R. Rodriguez, G. Mazza, Kinetic modeling of Co-Pyrogasification in municipal solid waste (MSW) management: towards sustainable resource recovery and energy generation, Sustainability 16 (10) (2024) 4056, https://doi.org/10.3390/su16104056.